JPhys Energy

TOPICAL REVIEW • OPEN ACCESS

The oxygen reduction reaction in solid oxide fuel cells: from kinetic parameters measurements to electrode design

Journal of Physics: Energy

Topical Review

The oxygen reduction reaction in solid oxide fuel cells: from kinetic parameters measurements to electrode design

Julián Ascolani-Yael[1], Alejandra Montenegro-Hernández[1], Diana Garcés[2], Quinyuan Liu[3], Hongqian Wang[3], Kyle Yakal-Kremski[3], Scott Barnett[3] and Liliana Mogni[1]

[1] INN-CNEA-CONICET, Centro Atómico Bariloche, Av. Bustillo 9500, S. C. de Bariloche, Rio Negro 8400, Argentina
[2] INN-CNEA, Centro Atómico Constituyentes-Instituto de Nanociencia y Nanotecnología, San Martin B1650KNA, Argentina
[3] Department of Materials Science and Engineering, Northwestern University, Evanston, IL 60208, United States of America

E-mail: julian.ascolani@cab.cnea.gov.ar **and** mogni@cab.cnea.gov.ar

Keywords: solid oxide fuel cell, cathode, O-ion diffusion coefficient, surface exchange

OPEN ACCESS

RECEIVED
8 April 2020

REVISED
11 June 2020

ACCEPTED FOR PUBLICATION
3 September 2020

PUBLISHED
7 October 2020

Abstract

The research and development of new Solid Oxide Fuel Cell cathode materials is an area of intense activity. The kinetic coefficients describing the O_2-reduction mechanism are the O-ion diffusion ($\boldsymbol{D}_{chem}$) and the O-surface exchange coefficients ($\boldsymbol{k}_{chem}$). These parameters are strongly dependent on the nature of the material, both on its bulk and surface atomic and electronic structures. This review discusses the method for obtaining the kinetic coefficients through the combination of electrochemical impedance spectroscopy with focused ion-beam 3D tomography measurements on porous electrodes (3DT-EIS). The data, together with oxygen non-stoichiometry thermodynamic data, is analysed using the Adler-Lane-Steele model for macro-homogeneous porous electrodes. The results for different families of oxides are compared: single- and double-layered perovskites with O-vacancies defects, based on La-Sr cobalt ferrites ($La_{0.6}Sr_{0.4}Co_{1-x}Fe_xO_{3-\delta}$, $x = 0.2$ and 0.8) and La/Pr-Ba cobaltites ($La_{0.5-x}Pr_xBa_{0.5}CoO_{3-\delta}$, $x = 0.0$, 0.2 and 0.5), as well as Ruddlesden-Popper nickelates ($Nd_2NiO_{4+\delta}$) with O-interstitial defects. The analysis of the evolution of molar surface exchange rates with oxygen partial pressure provides information about the mechanisms limiting the O_2-surface reaction, which generally is *dissociative adsorption* or *dissociation-limited*. At 700 °C in air, the La-Ba cobaltite structures, $La_{0.5-x}Pr_xBa_{0.5}CoO_{3-\delta}$, feature the most active surfaces ($\boldsymbol{k}_{chem} \simeq 0.5$–$1\ 10^{-2}$ cm.s^{-1}), followed by the nickelate $Nd_2NiO_{4+\delta}$ and the La-Sr cobalt ferrites, with $\boldsymbol{k}_{chem} \simeq 1$–$5\ 10^{-5}$ cm.s^{-1}. The diffusion coefficients $\boldsymbol{D}_{chem}$ are higher for cubic perovskites than for the layered ones. For $La_{0.6}Sr_{0.4}Co_{0.8}Fe_{0.2}O_{3-\delta}$ and $La_{0.6}Sr_{0.4}Co_{0.2}Fe_{0.8}O_{3-\delta}$, $\boldsymbol{D}_{chem}$ is 2.6 10^{-6} cm^2.s^{-1} and 5.4 10^{-7} cm^2.s^{-1}, respectively. These values are comparable to $\boldsymbol{D}_{chem} = 1.2\ 10^{-6}$ cm^2.s^{-1}, observed for $La_{0.5}Ba_{0.5}CoO_{3-\delta}$. The layered structure drastically reduces the O-ion bulk diffusion, e.g. $\boldsymbol{D}_{chem} = 1.3\ 10^{-8}$ cm^2.s^{-1} for the $Pr_{0.5}Ba_{0.5}CoO_{3-\delta}$ double perovskite and $\boldsymbol{D}_{chem} \simeq 2\ 10^{-7}$cm^2.s^{-1} for $Nd_2NiO_{4+\delta}$. Finally, the analysis of the time evolution of the electrodes shows that the surface cation segregation affects both the O-ion bulk diffusion and the surface exchange rates.

Nomenclature

SOFC	solid oxide fuel cells.
MIEC	mixed ionic and electronic conductor.
ORR	O_2 reduction reaction.
IEDP	Isotope Exchange Depth Profile.
ECR	Electrical Conductivity Relaxation.
EIS	Electrochemical Impedance Spectroscopy.
ALS	Adler-Lane-Steele model.
TLM	transmission line model.

LSCF	$= La_{0.6}Sr_{0.4}Co_{1-x}Fe_xO_{3-\delta}$
LSCF6482	$= La_{0.6}Sr_{0.4}Co_{0.8}Fe_{0.2}O_{3-\delta}$
LSCF6428	$= La_{0.6}Sr_{0.4}Co_{0.2}Fe_{0.8}O_{3-\delta}$
LPBC	$= La_{0.5-x}Pr_xBa_{0.5}CoO_{3-\delta}$
LPBC	$(x=0) = La_{0.5}Ba_{0.5}CoO_{3-\delta}$
LPBC	$(x=0.5) = Pr_{0.5}Ba_{0.5}CoO_{3-\delta}$
NNO	$= Nd_2NiO_{4+\delta}$
NNO-P	$= Nd_2NiO_{4+\delta}$ obtained by Pechini method.
NNO-SG	$= Nd_2NiO_{4+\delta}$ obtained by Sol-Gel method.
D_{chem}	O-ion chemical diffusion.
k_{chem}	O-surface chemical exchange coefficients.
D^*	O-isotope labeled or tracer diffusion coefficient.
k^*	O-isotope labeled or tracer surface exchange coefficient.
D_δ	defect diffusion coefficients for O-vacancies or O-interstitials.
k_δ	O-defects surface exchange coefficient for O-vacancies or O-interstitials.
D	diffusion coefficient.
k	surface exchange coefficient.
δ	oxygen defects, vacancies or interstitials.
x_δ^0	molar fraction of O-defects at equilibrium.
$A_O = \pm\frac{1}{2RT}\frac{\partial\mu_{O_2}}{\partial ln\delta}$	thermodynamic factors for oxygen vacancies $(-)$ or interstitials $(+)$.
μ_{O_2}, μ_δ^0	molecular and atomic defect chemical potentials.
Z_G	Gerischer impedance.
R_G	Gerischer resistance.
τ_G	Gerischer time constant.
a	specific surface area.
ε	porosity.
τ	solid-phase tortuosity factor.
c_δ	concentration of O-diffusive species.
λ	integer parameter related to the rate-limiting step.
$\Re_O$	equilibrium molar surface exchange rate.
Λ	free-energy driving force.
$G_{f,j}^0$	equilibrium free-energy barrier for step j.
ΔE_j	shift in free-energy of reaction.
Q_j	law of mass action corresponding to step j.
β_j	reaction symmetry parameter for step j.
c_i	concentration of reacting species.
c_O	concentration of oxygen lattice sites.
l_δ	characteristic utilization length.
$V_O^{\cdot\cdot}$	O-vacancy.
$O_O^\times$	O^{-2} ion in the O-sublattice.
$h^\cdot$	electron-hole.
e'	electron charge carrier.
pO_2	oxygen partial pressure.
fO_2	oxygen fugacity in the solid.
q_j	fraction of charge involved in the individual step j.
$s_{\delta,surf}$	surface site for adsorption.
$O_2^{-q_{ads},s}$	molecular O-adsorbed.
$O^{-q_{dis},s}$	atomic O-adsorbed.
$g(E_F)$	density of states at the Fermi level.
s_i	empty interstitial site.
O_i''	interstitial oxygen.
c_{s_i}	molar concentrations of empty oxygen interstitial sites.
N	number of O-interstitial sites by unit cell.
L	electrode thickness.
R_d	diffusion resistance.
R_s	distributed surface resistance.
Q_s	surface capacitance.

1. Introduction

The O_2 reduction reaction (ORR) taking place on the surface of a solid material is a relevant reaction for energy conversion and storage systems such as solid oxide fuel cells (SOFC), gas separation membranes, and metal-air batteries. Considerable research activities are aiming to increase the comprehension of ORR mechanisms, because the efficiency of these devices is limited by the cathodic polarization resistance—and

the associated overpotentials—especially when the operation temperature is reduced. Decreasing the operation temperature below 700 °C is important to improve the stability of the materials and reduce balance of plant costs, as is needed reaching a more widespread application of this technology. In order to achieve the reduction of the ORR overpotential of the cathode it is of crucial importance to understand the associated electrochemical processes. There are different electrochemical paths proposed depending on the capability of the solid to adsorb, incorporate, transfer charge or transport O-species, shown in a simplified scheme in figure 1. Generally speaking, the ORR mechanism involves O_2 gas transport, different alternatives of physisorption or chemisorption of either diatomic or atomic surface species ($O_2^s, O_2^{-,s}, O^{q-,s}$), total or partial charge transfer ($qe-$) to the O-species, surface or bulk diffusion of O-species through the solid ($O_2^s, O_2^{-,s}, O^{q-,s}, O^{q-}, O^{2-}\ with\ q<1$) and O-ion incorporation or transfer. The process that is the ORR rate limiting step depends on the characteristics of the specific cathode material. All steps involving surface process as physisorption, chemisorption, molecular dissociation, O-ion incorporation, including or not charge transfer, are well described by specific surface exchange coefficients (k_{chem}). Whereas the O-species diffusion in the solid, either on the surface or bulk are described by an oxygen diffusion coefficient (D_{chem}). Then, the so called 'kinetic parameters', D_{chem} and k_{chem} coefficients, are accepted parameters for describing the ability of a material to transport oxygen and thereby facilitate the ORR.

In this work we analysed the applicability of the 3DT-EIS method and we compared the results for different families of oxides: single- and double-layered perovskites with O-vacancies defects, based on La-Sr cobalt ferrites ($La_{0.6}Sr_{0.4}Co_{1-x}Fe_xO_{3-\delta}$, $x = 0.2$ and 0.8) and La/Pr-Ba cobaltites ($La_{0.5-x}Pr_xBa_{0.5}CoO_{3-\delta}$, $x = 0.0$, 0.2 and 0.5), as well as Ruddlesden-Popper nickelates ($Nd_2NiO_{4+\delta}$) with O-interstitial defects. These materials have received a lot of attention as cathodes due to their properties. $La_{0.6}Sr_{0.4}Co_{1-x}Fe_xO_{3-\delta}$ (LSCF) is a state-of-the-art mixed ionic and electronic conductor (MIEC) perovskite cathode [1], which shows ionic conductivity through an O-vacancy mechanism, high structural stability and presents low ASR values [2–5]. Also, it has a high degradation rate [6, 7], as a consequence of Sr segregation. Although this is a very much studied material, there is still considerable research being conducted on it, with the aim of decreasing degradation rates and improving the electrochemical activity. Recent experimental and theoretical studies have highlighted the potential of perovskite oxides $LnBaCo_2O_{6-\delta}$ (Ln = lanthanide), as candidate materials for intermediate temperature (600 °C–800 °C) solid oxide fuel cells (IT-SOFC) cathodes and oxygen separation membranes [8–11]. These materials show high rates of oxygen surface exchange [12] and diffusivity [13], and high electrical conductivity [14, 15]. However, there is not enough information about Ba-segregation in Ba-cobaltite porous electrodes. In these perovskites, the Ba plays a key role since its large cation radii mismatch also distorts the cubic crystal structure promoting the oxygen vacancy formation and migration [16], thus reducing the R_{tot} due to the improvement of the O-surface exchange and the O-ion diffusion. $La_{0.5-x}Pr_xBa_{0.5}CoO_{3-\delta}$, LPBC, cobaltites present a phase transition when substituting La for Pr, producing a change from isotropic to anisotopic ionic conductivity through an O-vacancy mechanism. This materials family presents low ASR, but a high rate of degradation, due to Ba segregation. Conversely, the $Nd_2NiO_{4+\delta}$ is Ba and Sr-free material, which helps disabling the degradation by cation segregation, and is also a Co-free material, an advantage in economic and other terms. This material belongs to the Ruddlesden-Popper phase with K_2NiF_4-type structure, which conducts oxygen through interstitials, has similar values of thermal expansion coefficients to those of electrolyte materials [17, 18] and presents thermal stability and chemical compatibility with $La_{0.9}Sr_{0.1}Ga_{0.8}Mg_{0.2}O_{2.85}$ (LSGM) electrolytes [19].

Although in this work the 3DT-EIS method is applied to these three types of materials, they represent a wide range of structures, chemical compositions and electrochemical behaviours and it should be noted that this method is applicable to any kind of MIEC materials.

1.1. The kinetic parameters

There are different techniques to measure the kinetic parameters, each one with its advantages and disadvantages. The two most widely used ones are $^{18}O/^{16}O$ isotope exchange depth profile (IEDP) [20–22] and Electrical Conductivity Relaxation (ECR) [23–26]. The kinetic coefficients reported by the IEDP method refer to the kinetics of O-isotope-labeled (^{18}O) species, D* and k*; whereas ECR measurements determine the kinetic parameters from the response to an applied chemical potential gradient, yielding the chemical kinetic diffusion coefficients, which are usually called 'chemical' (D_{chem} and k_{chem}) or 'O-defect' coefficients (D_δ and k_δ, where δ refers to O-defects, either O-vacancies or O-interstitials). Fortunately, there is a known relation between the different kinds of coefficients, as discussed below.

Both IEDP and ECR offer the advantage of using either polycrystalline or monocrystalline samples. Polycrystals are more realistic since actual electrodes are polycrystals, but they make calculations and data interpretation more difficult. On the contrary, by analyzing monocrystalline samples, it is possible to obtain detailed information about the effect of the surface and bulk crystallographic orientation on the ORR. As an example, Riva *et al* [27] studied monocrystalline Nb-doped $SrTiO_3$ samples by doing atomic-resolution STM

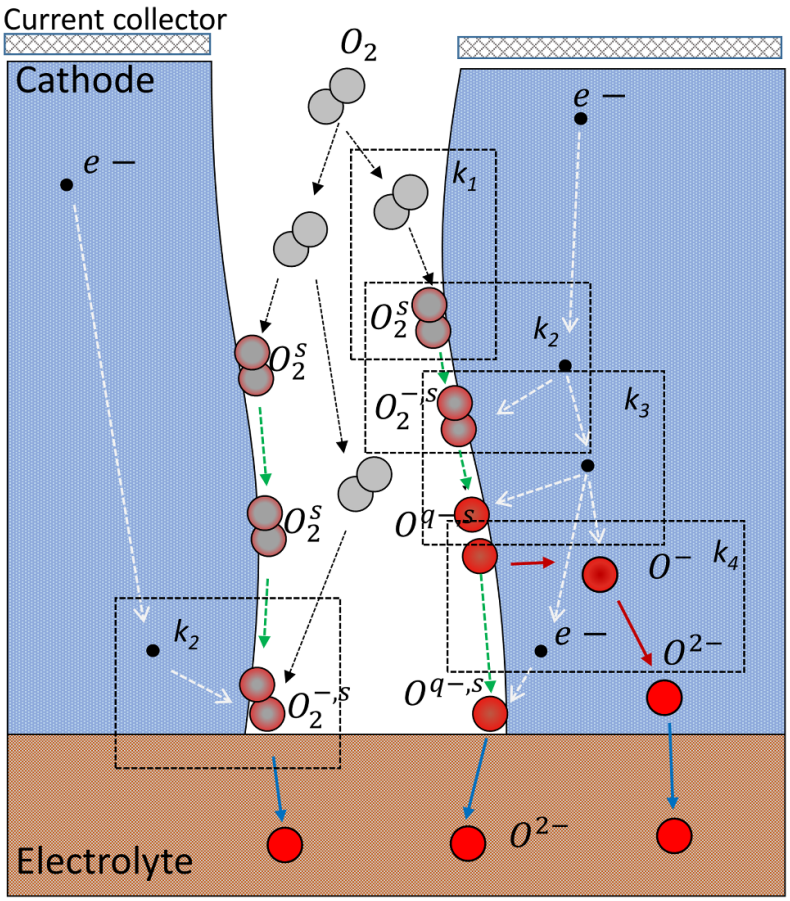

Figure 1. Alternative paths for the ORR in the electrode considering the oxygen diffusion in the gas phase (⇢), followed by multiple steps associated to surface exchange rates (e.g. k) and the diffusion of O-species (D), until the final O-ion transfer to the electrolyte (→). Surface exchange rate involves several possibilities such as physisorption (k_1), chemisorption (k_2), dissociation (k_3), and incorporation (k_4), with single or multiple charge transfer process (⇢); whereas the diffusion of O-species would take place inside the oxide (O-bulk diffusion, →) or at the surface of the oxide (O-surface diffusion, ⇢). The different O-species involved are molecular O_2 in gas phase; surface adsorbed species such as: physisorbed O_2^s, superoxides $O_2^{-,s}$ and adsorbed O-atomic $O^{q-,s}$ ($0 \leq q \leq 2$); also inside the solid oxide can be found other species such as peroxide ions O^-, O-ions O^{2-} and charge carriers such as electrons $e-$ •. Note that, the surface exchange rates can be experimentally determined (e.g. k_{chem}) despite the nature of the rate-limiting surface process would be unclear.

surface analysis and IEDP measurements, obtaining different values of oxygen incorporation rate depending on the crystalline orientation of the surface exposed to O_2.

Since both techniques need dense samples to carry out the experiments, unfortunately, it is not always an easy task to obtain single crystals with the adequate dimensions for IEDP and ECR experiments. For both, IEDP and ECR, the sample dimensions must be large enough to prevent the crossing of the concentration profiles in the center of the sample during the tracer annealing time, otherwise, the boundary conditions used in modelling the results might not be fulfilled [20]. Besides, the smallest dimension of IEDP or conductivity relaxation samples should be close to the characteristic distance, defined as: $l = \frac{D}{k}$. If the ratio D/k is much lower than the sample dimensions, the results for D are accurate, but k will have considerable error. Conversely, if D/k is larger than the sample dimension, then k can be obtained accurately but D will have considerable inaccuracy [23]. ECR measurements can be performed on porous samples, but the accuracy in the determination of D and k depends heavily on the sample thickness [26]. Furthermore, the particle size for this method is typically much larger than D/k, so it can be difficult to measure k accurately. Thus, in IEDP and conductivity relaxation methods it may be necessary to employ multiple samples with different dimensions to obtain the kinetic parameters over the range of temperatures T and oxygen partial pressure pO_2 of interest.

Another drawback is that the fabrication of dense pellets requires much higher firing temperatures than those used for preparing real porous electrodes, producing uncontrolled changes in the nature of the material, such as surface segregation. These uncontrolled alterations can modify the measured exchange rate

coefficients as much as an order of magnitude [28]. These kinds of experiments have very precise interpretations for the processes involved and allow computational modelling of the surface reactivity at the first-principles level. Nevertheless, they fail to represent a real porous electrode material, given that this approach does not take into account effects generated by surface curvature, surface composition, the sometimes nano-sized nature of the grains, surface segregation of species, etc.

An alternative solution for obtaining results that are more indicative of real electrodes was proposed by S B Adler's group [29]. They analysed the electrochemical response of one electrode, measured by Electrochemical Impedance Spectroscopy (EIS), in the frame of a semi-infinite macro-homogeneous porous electrode by applying the so called Adler-Lane-Steele (ALS) model [30, 31]. The ALS model includes microstructural information that can be obtained by 3D tomography methods such as FIB-SEM [32–35], and thermodynamic information about O-defect concentration. The kinetic coefficients can be obtained by using this data in conjunction with fits to EIS spectra. In this work we will refer to the combination of 3D tomography with EIS data to obtain kinetic information as 3DT-EIS.

The main drawback of this approach is that it requires the use of advanced 3D tomographic characterization of the electrode microstructure. However, 3D tomography has been successfully applied to the study of a wide range of porous SOFC electrodes, from anode composites, e.g. Ni–YSZ (YSZ is Y stabilized ZrO_2) [32, 36], Ni-GDC (GDC is Gd–doped CeO_2) [37], Ni–ScSZ (ScSZ is Sc– stabilized ZrO_2) [38]; infiltrated nanoscaled anodes, e.g. LSM infiltrated on YSZ scaffold [39], or single phase cathodes such as La-Sr-Ba cobaltites or cobalt-ferrites [29, 40–46] or La–Sr–Ca manganites [47]. In the present context where the focus is on single-phase MIEC oxides, the relevant microstructural parameters are the solid and pore volume fractions, surface areas, and tortuosities. An important advantage of the 3DT-EIS method is that it takes into account time evolution effects, such as species segregation [1, 6, 42, 48, 49], surface reconstructions [50], studying the effect of volatile species, etc. Also, the data collection is relatively fast compared with the time needed for carrying out IEDP experiments and is comparable with the length of ECR experiments. Also, the 3DT-EIS method allows testing several temperatures and pO_2 conditions in a single experiment, simplifying the samples preparation and reducing experimental time. Finally, this method allows to obtain both k and D simultaneously, in contrast to IEDP and ECR, which allow to obtain only one parameter with good accuracy at a time. In short, the 3DT-EIS method opens up new possibilities to study a wide variety of samples, taking into account the real conditions in which these are characterized electrochemically. These possibilities allow for a direct correlation of the kinetic parameters to the electrode electrochemical properties and for an advanced design of electrode materials.

Table 1 shows a simplified comparison of the three methods presented in this work. The Sample Processing category represents the difficulty for preparing the samples, firing temperatures, quantity of samples needed. The Data Collection category mainly represents the time needed for carrying out the experiments and the difficulty of the experiments. The Data Processing category refers to the time needed and the difficulty of processing the acquired data and extracting the desired information. Finally, the Accuracy category refers to the accuracy of the method, in the statistical sense of distance of the extracted values to the 'true' values, related to the real conditions and characteristics of the electrode, and the independency on the determination of k and D. The closer the measured values to the 'true' values are, the better the accuracy of the method.

In this work, we discuss recent results obtained using 3DT-EIS to analyse the properties and performance of different SOFC porous electrodes, such as double perovskites based on La-Sr cobalt ferrites ($La_{0.6}Sr_{0.4}Co_{1-x}Fe_xO_{3-\delta}$, x = 0.2 and 0.8) and La/Pr-Ba cobaltites ($La_{0.5-x}Pr_xBa_{0.5}CoO_{3-\delta}$, x = 0.0, 0.2 and 0.5), as well as Ruddlesden-Popper nickelates ($Nd_2NiO_{4+\delta}$) with O-interstitial defects.

Also, modifications to adapt the electrochemical model from semi-infinite to finite-length electrodes are discussed. The mechanisms of surface reaction and O-ion diffusion are proposed from analysing the behaviour of the kinetic parameters with the O_2 partial pressure. In order to facilitate the comparison, the following relationships between the kinetic coefficients obtained by different techniques are used:

$$D_{chem} = D_\delta A = \frac{D^* A}{x_\delta^0} \tag{1}$$

and

$$k_{chem} = k_\delta A = \frac{k^* A}{x_\delta^0} \tag{2}$$

where $A = (+/-)\frac{1}{2RT}\frac{\partial \mu_{O_2}}{\partial ln x_\delta}$ is the thermodynamic factor describing how oxygen non-stoichiometry varies with oxygen chemical potential (μ_{O_2}), with the $(-)$ sign corresponding to O-vacancies and $(+)$ sign to O-interstitials, R is the universal gas constant, T is the absolute temperature and the factor 1/2 is included to

Table 1. Schematics of the strengths and weaknesses of the three methods commonly used for obtaining the kinetic coefficients. For the sample processing category, the difficulty for preparing the samples, firing temperatures, quantity of samples needed, were taken into account. The data collection category represents the time needed for carrying out the experiments and the difficulty of these experiments. The data processing category refers to the time needed and the difficulty of processing the acquired data. The accuracy category represents the overall accuracy of the methods, based mainly on how representative are the samples of real SOFC electrodes and of the conditions of real operating devices. The yellower the disk is, the better the performance of the method.

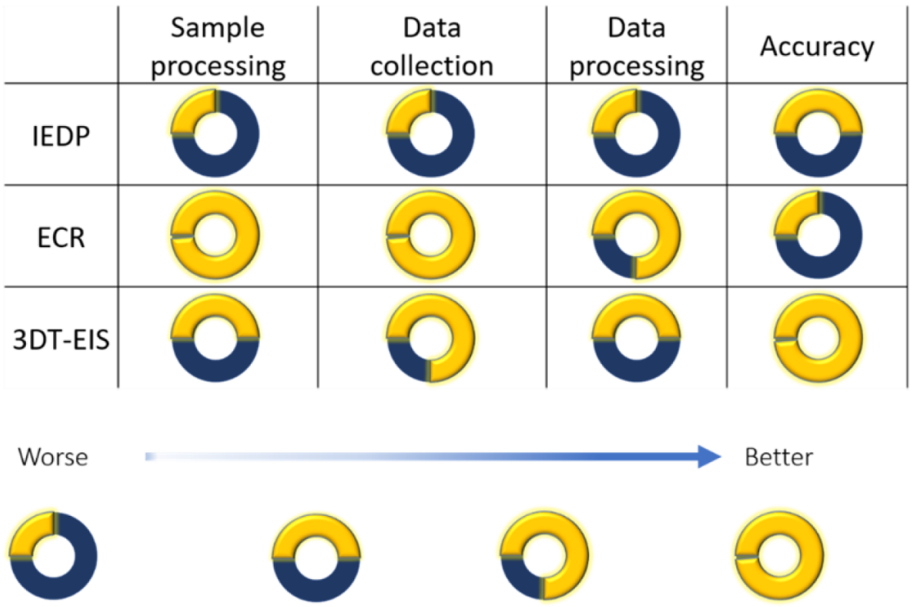

take into consideration the relationship between molecular μ_{O_2} and the atomic O-chemical potential in the solid ($\mu_O = \mu_{O_2}/2$) and x_δ^0 is the molar fraction of O-defects at equilibrium, e.g.: for an electrode with perovskite structure ($ABO_{3-\delta}$), $x_\delta^0 = \delta_{eqb}/3$ that means that in the equilibrium, it distributes the O-vacancies (δ_{eqb}) in the 3 sites of O available per mol of perovskite.

1.2. The ALS model for semi-infinite porous electrodes

The ALS model is used to describe the response of a porous single phase MIEC electrode, whose EIS spectra can be fitted by a Gerischer type impedance [29]:

$$Z_G = R_G \frac{1}{\sqrt{1 + j\omega\tau_G}} \tag{3}$$

where R_G is the resistance and τ_G the time constant. Although the model specifies a case where the ionic conductivity is dominated by O-vacancy species in the bulk of the MIEC, the same basic framework can be extended to O-interstitial or surface diffusion conduction mechanisms. The basic idea of this model is to solve the differential equation for 1D diffusion for an O-active species in a porous macro-homogeneous medium, which means that its microstructure can be described by average parameters, such as the electrode specific surface area a, porosity ε and the solid-phase tortuosity factor τ, the latter defined as the ratio between the effective path length traveled by the diffusive species to the straight distance $\tau = \frac{L_{ef}}{L}$. Under these conditions, the following diffusion equation is valid:

$$(1-\varepsilon)\frac{\partial c_\delta(x,t)}{\partial t} = \frac{(1-\varepsilon)}{\tau} A D_\delta \frac{\partial^2 c_\delta(x,t)}{\partial x^2} - ar \tag{4}$$

where c_δ is the concentration of O-diffusive species, and D_δ its diffusion coefficient. In this equation the diffusion is coupled or *co-limited* with a surface reaction (r), given that it also changes $c_\delta(x,t)$. The net O_2 reduction rate at the surface (r) can be analysed in the frame of transition state theory, with a nonequilibrium thermodynamic rate expression:

$$r = \Re_o \left[1 - e^{-\Lambda/\lambda RT}\right] \tag{5}$$

where λ is an integer parameter related to the rate-limiting step, $\Re_o$ is the oxygen molar equilibrium surface rate and Λ is the free-energy driving force for the limiting mechanism controlling the surface process. As discussed above, the oxygen surface exchange involves a series of steps such as adsorption of O_2 molecules from the gas phase, dissociation of these molecules, incorporation of the O-atoms into the MIEC bulk, etc.

Then, the driving force for each individual step (Λ_j) is the difference in chemical potential of the reaction in the framework of nonequilibrium thermodynamics:

$$\Lambda_j = \Delta\mu_j = \Delta\mu_j^0 + RTlnQ_j + \Delta E_j \tag{6}$$

and the net rate of any elementary reaction step j is

$$r_j = k_j e^{-\frac{\Delta G_{f,j}^0}{RT}} e^{-\frac{\left(1-\beta_j\right)\Delta E_j}{RT}} \left[1 - e^{-\frac{\Lambda_j}{RT}}\right] \prod_i c_i = \Re_{o,j}\left[1 - e^{-\Lambda_j/\lambda_j RT}\right] \tag{7}$$

where $\Delta G_{f,j}^0$ is the equilibrium free-energy barrier for step j, ΔE_j is a shift in free-energy of reaction associated to the driving force, Q_j is the law of mass action corresponding to step j, β_j is a reaction symmetry parameter (analogous to the one used in electrochemical kinetics) and c_i are the concentration of reacting species in the forward direction of the *j*-step. In the equilibrium limit ($\Lambda_j \to 0$) and small perturbations, the linearization of equation (7) is possible and $\Re_o$ becomes the exchange rate, which can be estimated as:

$$\Re_o = \lambda RT\left(\frac{\partial r}{\partial \Lambda}\right)_T = -\lambda\frac{c_\delta}{A}\left(\frac{\partial r}{\partial c_\delta}\right)_T = \Re_o\left(T, pO_2\right) \tag{8}$$

where A is the thermodynamic factor defined above. Thus, in general: $\Re_o = k_\delta c_\delta pO_2^{n'}$ or $\Re_o \propto pO_2^n$, where the dependence of $\Re_o$with pO_2 gives an indication of the limiting mechanism of the surface reaction. A more detailed discussion about the surface oxygen-exchange reaction can be found in [51]. and in section 1.2.

Besides solving the solid phase diffusion equation (equation (4)), the ALS model solves the O_2-gas diffusion in gas phase (both inside the porous material and in the boundary layer) and the equation considering the interfacial charge-transfer reactions occurring at the mixed conductor/electrolyte interface (O-ion transfer, $i_{O^{-2}}$) and the mixed conductor/current-collector interface (e^- transfer, i_{e-} [30, 31]). The solution of the diffusion problem with adequate boundary conditions, e.g.: $c_\delta(x = L, t > 0) = c_\delta^0$ and $c_\delta\left(x = 0, t\right) = c_\delta^0 + \Delta c_\delta cos\left(\omega t\right)$, predicts that the zero-bias impedance of a symmetrical cell (electrode/electrolyte/electrode) is the sum of the electrolyte resistance, a charge-transfer impedance (across electrolyte-electrode interfaces) and a 'chemical' impedance associated with non-charge transfer or chemical reaction processes:

$$Z = R_{el} + Z_{interface} + Z_{chem} \tag{9}$$

The Z_{chem} expression for a semi-infinite electrode, with non-charge-transfer processes, includes convoluted contributions of oxygen surface exchange and solid-state diffusion, and obeys a Gerischer-type impedance (equation (3)). Then, R_G and τ_G can be directly related to microstructural, thermodynamic and kinetic parameters by:

$$R_G = \frac{RT}{4F^2}\frac{1}{\sqrt{4a\Re_o c_O x_\delta^0 \frac{(1-\varepsilon)}{\tau} D_\delta}} \tag{10.1}$$

$$\tau_G = \frac{(1-\varepsilon)\, c_O x_\delta^0}{4a\Re_o A} \tag{10.2}$$

where c_O is the concentration of oxygen lattice sites involved in the diffusion mechanism, and the other parameters were already defined.

This model has a characteristic utilization length l_δ, defined as:

$$l_\delta = \sqrt{\frac{(1-\varepsilon)}{\tau}\frac{D_\delta c_O x_\delta^o}{4a\Re_o}} \tag{11}$$

The distance l_δ refers to the depth into the electrode (from the electrolyte) over which the reaction takes place ($\simeq 3l_\delta$). Inside this zone, the gradient of O^{2-} concentration ($i_{O^{2-}}$) is maximum, whereas outside it the concentration is constant.

Table 2. Microstructural parameters of porous electrodes obtained from 3D FIB-SEM reconstruction.

	Porosity (ε)	Solid phase tortuosity (τ)	Specific surf. area (a) (μm^{-1})
LSCF	0.42	1.24	6.87
LPBC	0.42	1.28	3.78
LPBC-aged	0.46	1.28	3.12
NNO-SG	0.54	1.18	4.96
NNO-P	0.54	1.50	1.57

1.3. The ALS model and mechanisms of surface reaction

The ALS model was developed for electrodes with O-vacancy defects. This means that the overall ORR (in the *Kröger–Vink* notation) is, for a p-type conductor, expressed as follows:

$$O_2^{gas} + 2V_O^{\cdot\cdot} \rightarrow 2O_O^{\times} + 4h^{\cdot} \tag{12}$$

or for an n-type conductor:

$$O_2^{gas} + 2V_O^{\cdot\cdot} + 4e' \rightarrow 2O_O^{\times} \tag{13}$$

where $V_O^{\cdot\cdot}$ refers to an O-vacancy, $O_O^{\times}$ to an O^{2-} ion in the O-sublattice and $h^{\cdot}$ or e' to an electron-hole or electron charge carrier, respectively. Given that perovskites used as O_2-electrodes typically exhibit p-type conductivity, the following is based on equation (12). In the equilibrium of the global reaction, the difference between the chemical potentials is zero:

$$\Delta\mu = 0 = \mu_{O_2}^{gas} - \mu_{O_2}^{sol} = \mu_{O_2}^{gas} + 2\left(\mu_{V_O^{\cdot\cdot}} - \mu_{O_O^{\times}} - 2\mu_{h^{\cdot}}\right) = RTln\frac{pO_2}{fO_2} \tag{14}$$

where pO_2 is the gas oxygen partial pressure and fO_2 the oxygen fugacity in the solid. Equation (14) gives a relationship between defect concentrations (c_δ) and pO_2 near to equilibrium conditions.

A specific mechanism can be proposed for the surface reaction with different steps, for example:

I. Adsorption $O_2^{gas} + s_{\delta,surf} \rightarrow O_2^{q-_{ads},s} + q_{ads}h^{\cdot}$

II. Dissociation $O_2^{q-_{ads},s} + s_{\delta,surf} \rightarrow 2O^{q-_{dis},s} + q_{dis}h^{\cdot}$

III. Incorporation $O^{q-_{dis},s} + V_O^{\cdot\cdot} \rightarrow O_O^{\times} + s_{\delta,surf} + q_{inc}h^{\cdot}$

where q_j is the fraction of charge involved in the individual step j ($j = ads, dis, inc.$ for adsorption, dissociation and incorporation, respectively; and $q_{ads} + q_{dis} + q_{inc} = 2$), $s_{\delta,surf}$ refers to a surface site for adsorption (e.g.: a surface O-vacancy), $O_2^{q-_{ads},s}$ and $O^{q-_{dis},s}$ refer to molecular and atomic O-adsorbed species, respectively.

Then, in the framework of non-equilibrium thermodynamics of equation (6), each individual step can be expressed considering the individual mass action law for $Q_j = \frac{\prod_i^{reactives} c_{i,j}}{\prod_n^{products} c_{n,j}}$ and the Rigid Band Model (RBM) formalism [52–54] for the relation $\Delta E_j = q_j \Delta E$. The RBM formalism considers itinerant charge carriers in a partially filled, wide, *M3d-O2p* band to estimate the contribution of charge carriers to the energy:

$$\Delta E = \mu_{e'} - \mu_{e'}^0 = \frac{4c_{e'}}{g(E_F)} \; or \; \Delta E = \mu_{h^{\cdot}} - \mu_{h^{\cdot}}^0 = \frac{4c_{h^{\cdot}}}{g(E_F)} \tag{15}$$

where $g(E_F)$ indicates the density of states at the Fermi level and, in the case of O-vacancy defects ($V_O^{\cdot\cdot}$), the relations $c_{e'} = 2c_\delta$ or $c_{h^{\cdot}} + 2c_\delta = c_{M'}$ are valid from electroneutrality balance.

Depending on which is the ORR limiting step, different expressions can be observed for $\Re_o$ (see equation (7)), which can be linearized in near equilibrium conditions (equation (8)) to obtain analytical expressions for $\Re_o = k_{chem}\frac{c_\delta}{A}pO_2^{n'}$. Note that c_δ and k_{chem} could also vary with pO_2 (see equations (7) and (14)), then the total pO_2 dependency is estimated as $n = \frac{\partial ln\Re_o}{\partial lnpO_2}$. Tables 2 and 3 from [51] summarize this information. Below, we discuss possible surface rate mechanisms, co-limiting with O-ion diffusion:

(a) *Chemisorption-limited* reaction (step I), the surface reaction is mediated by a highly unstable physisorbed diatomic intermediate, which is transformed to a more stable diatomic superoxide intermediate (O_2^-):

$$O_2^{gas} \overset{co-limiting}{\rightarrow} O_2^{-,s}.$$

This reaction is limited by an energy barrier and $n = \frac{1}{2} + \frac{q_{dis} - (1-2\beta_{ads})q_{adss}}{8}\left(1 - \frac{1}{A}\right)$, where $q_{ads} = 1$, $q_{dis} = 3$, $q_{inc} = 0$, $\beta_{ads} = 0.5$ or 1 for metals or p-type semiconductors, respectively. The molar surface exchange rate is expressed as $\Re_o = k_{chem}\frac{c_\delta}{A}pO_2^{n'}$ ($0.6 \lesssim n' \lesssim 1$).

Table 3. Measured diffusion coefficients (D_{chem}), molar exchange rates ($\Re_o$), surface exchange coefficients (k_{chem}) and activation energies (E_a) for the electrodes studied by our group: $La_{0.6}Sr_{0.4}Co_{1-x}Fe_xO_{3-\delta}$ (with $x = 0.2$ -LSCF6482- and $x = 0.8$ -LSCF6428-), $La_{0.5-x}Pr_xBa_{0.5}CoO_{3-\delta}$ (LPBC with $x = 0.0$, 0.2 and 0.5) and $Nd_2NiO_{4+\delta}$ (NNO-SG and NNO-P) electrodes. Also, information from literature reported for other electrodes, obtained with similar methodologies are included for comparison.

	D_{chem}			$\Re_o$			k_{chem} [1]	
	@ 700 °C air ($cm^2.s^{-1}$)	pO_2^m, m @700 °C	E_a (eV)	700 °C air ($mol.cm^{-2}.s^{-1}$)	pO_2^n, n 700 °C	E_a (eV)	700 °C ($cm.s^{-1}$)	
LSCF6428[2]	$5.4\ 10^{-7}$	0.5(high pO_2) 0.2(low pO_2)	−0.2	$3\ 10^{-9}$	0.3	1.5	$1.7\ 10^{-5}$	Our work
$La_{0.6}Sr_{0.4}Co_{0.2}Fe_{0.8}O_{3-\delta}$[2]	$2.8\ 10^{-7}$						$5.2\ 10^{-5}$	[42]
$La_{0.58}Sr_{0.4}Co_{0.2}Fe_{0.8}O_{3-\delta}$[3]							$1.8\ 10^{-2}$	[41]
$La_{0.8}Sr_{0.2}CoO_{3-\delta}$[3]	$1\ 10^{-6}$	0.8		$1.5\ 10^{-8}$	0			[29]
$La_{0.6}Sr_{0.4}CoO_{3-\delta}$[3]	$3.6\ 10^{-7}$	0	1.5	$1.5\ 10^{-7}$	0.5	0.46		[29]
LSCF6482	$2.6\ 10^{-6}$	0.2	1.2	$9\ 10^{-9}$	0.5	0.9	$3.6\ 10^{-5}$	Our work
$Ba_{0.5}Sr_{0.5}Co_{0.82}Fe_{0.2}O_{3-\delta}$[3]							$4.2\ 10^{-2}$	[41]
LPBC x = 0.0	$1.2\ 10^{-6}$	0	0.89	$2.1\ 10^{-6}$	0.5	1.27	$4.8\ 10^{-3}$	Our work
LPBC x = 0.2	$4.5\ 10^{-7}$	0	0.72	$4.8\ 10^{-6}$	0.25	1.34	$3.9\ 10^{-3}$	Our work
LPBC x = 0.5	$1.3\ 10^{-8}$	0	1.1	$2.6\ 10^{-6}$	0.6	0.9	$1.0\ 10^{-2}$	Our work
NNO-SG	$3.2\ 10^{-7}$	0	0.92	$2.6\ 10^{-8}$	0.75	1.38	$1.1\ 10^{-5}$	Our work
NNO-P[4]	$1.9\ 10^{-7}$	0	0.87	$4.6\ 10^{-8}$	0.5	1.3	$6.3\ 10^{-5}$	Our work

[1] k_{chem} is estimated from $\Re_0 = k_{chem} \frac{c_\delta}{A} pO_2^n$

[2] LSCF6428 also has a $\Re_0$ associated with the R_{LF}//CPE element. At 700 °C and $pO_2 = 0.02$ atm, $\Re_0 = 9.10^{-8}$ $mol.cm^{-2}.s^{-1}$, and it is $\propto pO_2^{3/4}$, $k_{chem} \simeq 2\ 10^{-4}$ $cm.s^{-1}$.

[3] Literature data adapted to D_{chem} and k_{chem} by using their thermodynamic data and applying equations (1) and (2).

[4] NNO-P $\Re_0$ associated with the R_{LF}//CPE element. At 700 °C $pO_2 = 0.01$ atm, $\Re_0 = 5.10^{-9}$ $mol.cm^{-2}.s^{-1}$, and it is $\propto pO_2^{1/2}$, $k_{chem} \simeq 1.6\ 10^{-5}$ $cm\ s^{-1}$.

(b) *Dissociation-limited* (step II), this step acquires importance when the *chemisorption* reaction is fast. This mechanism is mediated by an unstable diatomic superoxide intermediate that is transformed to a more stable single-atomic adsorbed intermediate, once an energetic activation barrier is overcome. Then $n = \frac{\beta_{dis} q_{dis}}{4}\left(1-\frac{1}{A}\right)$, $q_{ads}=1$, $q_{dis}=3$, $q_{inc}=0$ and $\beta_{dis}=0.5$,

$$O_2^{gas} \rightarrow O_2^{-,s} \overset{co-limiting}{\rightarrow} O^{2-,s}.$$

The molar surface exchange rate is also expressed as $\Re_o = k_{chem}\frac{c_\delta}{A} pO_2^{n'}$ $(0.25 \lesssim n' \lesssim 0.4)$.

(c) *Dissociative adsorption-limited* reaction. In this case the reaction is mediated by a highly unstable physisorbed diatomic intermediate, which is transformed to a more stable single-atomic adsorbed intermediate (step I and II collapse to a single step) and it is limited by the probability of finding a second vacancy near the diatomic intermediate. This reaction is limited by an entropy barrier and $n = \frac{\beta_{dis} q_{dis}}{4}\left(1-\frac{1}{A}\right)$, where $q_{ads}=0$, $q_{dis}=4$, $q_{inc}=0$ and $\beta_{dis}=1$,

$$O_2^{gas} \rightarrow O_2^{s} \overset{co-limiting}{\rightarrow} O^{2-,s}.$$

The molar surface exchange rate is expressed as $\Re_o = k_{chem}\frac{c_\delta}{A} pO_2^{n'}$ $(0.4 \lesssim n' \lesssim 0.75)$.

(d) *Incorporation-limited* (step III), this step occurs if the surface is equilibrated with the gas, steps I and II are fast and the reaction is limited by exchange of oxygen vacancies with the bulk. In that case $n = -\frac{1}{2A} - \frac{(1-\beta_{inc})q_{inc}}{4}\left(1-\frac{1}{A}\right)$, with $q_{ads}=1$, $q_{dis}=3$, $q_{inc}=0$,

$$O_2^{gas} \rightarrow O_2^{-,s} \rightarrow O^{2-,s} \overset{co-limiting}{\rightarrow} O^{2-}.$$

The molar surface exchange rate in this case is $\Re_o = k_{chem}\frac{c_\delta}{A} pO_2^{n'}$, $(-0.25 \lesssim n' \lesssim 0)$.

According to the reactions expressed in equations (12) and (13), the diffusive species in equation (4) is an O-ion with a mechanism of O-vacancies ($V_O^{\cdot\cdot}$); and the surface reaction mechanism involves steps I to III, then the O-ion diffusion happens once the O-ion is incorporated into the bulk of the non-stoichiometric oxide. Therefore, in this O-ion bulk diffusion mechanism it is expected that as pO_2 decreases, the concentration of $V_O^{\cdot\cdot}$ should increase, and hence a slight decrease of the contribution of bulk diffusion polarization resistance is also expected in EIS experiments. However, if the surface reaction is strongly *dissociation* or *incorporation-limited*, O_2^s, $O_2^{-,s}$, $O^{-,s}$ or $O^{2-,s}$ species can be accumulated on the surface, making a diffusion path through the surface possible. In these cases, as pO_2 decreases, the concentration of diffusive species decreases and, as a consequence, the contribution of surface diffusion polarization resistance increases. The strong increment of D_{chem} with increasing pO_2 is an evidence of the superficial character of O-diffusion, as it was suggested by Lu *et al* [29] for La-rich cobaltite porous electrodes .

1.4. The ALS model for different kinds of O-lattice defects

All of the above discussion was proposed for electrodes with O-vacancy defects. However, there are also MIEC electrodes where the O-defects consist of extra O-atoms located in interstitials sites. In those cases, equation (12) must be re-written as:

$$O_2 + 2s_i \rightleftharpoons 2O''_i + 4h^{\cdot} \tag{16}$$

where s_i is an empty interstitial site and O_i'' is an oxygen ion located in the interstitial site. In this case, c_δ refers to the molar concentration of O-interstitials.

Following the same concepts as for O-vacancies, a possible mechanism for the surface reaction could be:

IV. Adsorption $O_2^{gas} + s_{i,surf} \rightarrow O_2^{q-_{ads},s} + q_{ads}h^{\cdot}$

V. Dissociation $O_2^{q-_{ads},s} + s_{i,surf} \rightarrow 2O^{q-_{ads},s} + q_{dis}h^{\cdot}$

VI. Incorporation $O^{q-_{dis},s} + s_{i,bulk} \rightarrow O_i'' + s_{i,surf} + q_{inc}h^{\cdot}$

For O-interstitial defects, the adsorption and dissociation steps are similar to those for O-vacancy defects. Then, an analogous analysis with similar results can be observed for *chemisorption, dissociative adsorption* or *dissociation-limited* reactions, with the consideration that c_δ must be replaced by c_{s_i}, the concentration of empty O-interstitial sites. Note that $c_\delta + c_{s_i} = \frac{N}{V_{u.c.}}$, where N is the number of O-interstitial sites by unit cell.

Also, the electroneutrality balance requires that $c_{h^{\cdot}} = 2c_{\delta}$, which modifies the RBM energy expression and equilibrium condition (equation (14)) to:

$$\Delta\mu = 0 = \mu^{gas}_{O_2} + 2\left(\mu_{s_i} - \mu_{O_i''} - 2\mu_{h^{\cdot}}\right) = RTln\frac{pO_2}{fO_2} \tag{17}$$

Then, the relation $\Re_o \simeq k_{chem}\frac{c_{s_i}}{A}pO_2^{n'}$ is also valid. However, a few corrections must be included by considering the different sign of the thermodynamic factor depending on whether the defects are vacancies, $A = (-)\frac{1}{2RT}\frac{\partial\mu_{O_2}}{\partial lnx_{\delta}}$, or interstitials, $A = (+)\frac{1}{2RT}\frac{\partial\mu_{O_2}}{\partial lnx_{\delta}}$. Then, for *Chemisorption* and *Dissociation-limited* mechanisms $n = \frac{1}{2} + \frac{q_{dis}-(1-2\beta_{ads})q_{adss}}{8}\left(1+\frac{1}{A}\right)$ and $n = \frac{\beta_{dis}q_{dis}}{4}\left(1+\frac{1}{A}\right)$, respectively. For the case where the reaction is *incorporation-limited*, a similar analysis to that performed in [51] indicates that $n = -\frac{(1-\beta_{inc})q_{inc}}{4}\left(1+\frac{1}{A}\right)$. In this case, the diffusive species is an O-ion by a mechanism of O-interstitials (O_i''), which decreases its concentration as pO_2 decreases, and as a consequence the diffusion polarization resistance is expected to increase.

In summary, from the analysis of $n = \frac{\partial ln\Re_o}{\partial lnpO_2}$, a surface exchange limiting reaction can be suggested; e.g.: considering an ORR involving O-vacancies formation with a mechanism following steps I-II-III, and $q_{ads} = 1, q_{dis} = 3, q_{inc} = 0, \beta_{ads} = 1, \beta_{inc} = 0.5 n_{chemisorption} > n_{dissociative-adsorption} > n_{dissociation} > n_{incorporation}$. This analysis would be reinforced by considering the diffusion coefficient and its dependence with pO_2 ($m = \frac{\partial lnD_{chem}}{\partial lnpO_2}$) together with complementary thermodynamic data indicating the relation between defects concentration and pO_2. Once the limiting-step is determined, k_{chem} can be estimated from the relation $\Re_o \simeq k_{chem}\frac{c_{\delta}}{A}pO_2^{n'}$. Thus, k_{chem} and D_{chem} obtained for real porous electrodes in this way provides helpful information to improve electrode materials design by comparing materials with different crystallographic structures, compositions, microstructures, also for understanding degradation mechanisms, obtaining information about the effect of functionalized surfaces, etc.

The ALS model described by equations (10.1) and (10.2) is valid as long as two hypotheses hold true: (1) the electrode length can be approximated as semi-infinite, meaning that the electrode thickness (L) is much larger than the characteristic utilization length ($L \gg 3l_{\delta}$) and (2) the electrode is macro-homogeneous, meaning that $3l_{\delta}$ must be higher than the size of some characteristic morphological features, e.g.: the average particle diameter.

For the cases where the semi-infinite electrode condition fails, a simple modification can be done to the ALS model to describe the finite nature of the electrode.

1.5. The ALS model for a finite length porous electrode

Finite-length electrodes, where the electrode reaction takes place along the total electrode thickness ($L \simeq l_{\delta}$), are usually well modeled by a transmission line model (TLM) [6, 55]. The TLM was developed for electrodes characterized by two percolated networks of ionic and electronic conducting materials and it was applied to describe either composites, infiltrated and MIEC electrodes. In the particular case where the electronic conduction is much larger than the ionic conduction, the TLM is described by a distributed diffusion resistance (R_d) a distributed surface resistance (R_s), a surface capacitance (Q_s) and a time distribution exponent (α) as:

$$Z_{TLM} = \sqrt{R_dR_s}\sqrt{\frac{1}{1+R_sQ_s(j\omega)^{\alpha}}}coth\left(\sqrt{\frac{R_d}{R_s}}\sqrt{1+R_sQ_s(j\omega)^{\alpha}}\right) \tag{18}$$

Figure 2 shows the Nyquist representation of the TLM element in different regimes. The limits where the diffusion resistance is much higher than the surface resistance ($R_d \gg R_s or L \gg l_{\delta}$) the TLM transforms to a Gersicher-like spectrum (figure 2(a)). As surface resistance increases, or $L \sim l_{\delta}$, a two arc spectrum typical of TLM appears (figure 2(b)). In this condition, the high frequency part of the spectrum is dominated by the diffusion process, while the low frequency part of the spectrum is dominated by the surface process (this can be changed depending on the value of Q_s). Finally, it can be noted that in the limit of large surface reaction resistance, or large utilization length $L \ll l_{\delta}$, equation (18) transforms to an R//CPE like element (figure 2(c)) [31, 56].

Taking this into account it can be shown that $Z_{TLM} \rightarrow Z_G$ in the limit of $L \gg l_{\delta}$, and the following identifications with the Gerischer impedance parameters can be established [57]:

$$R_G \approx \sqrt{R_dR_s} \tag{19.1}$$

$$\tau_G \approx R_sQ_s \tag{19.2}$$

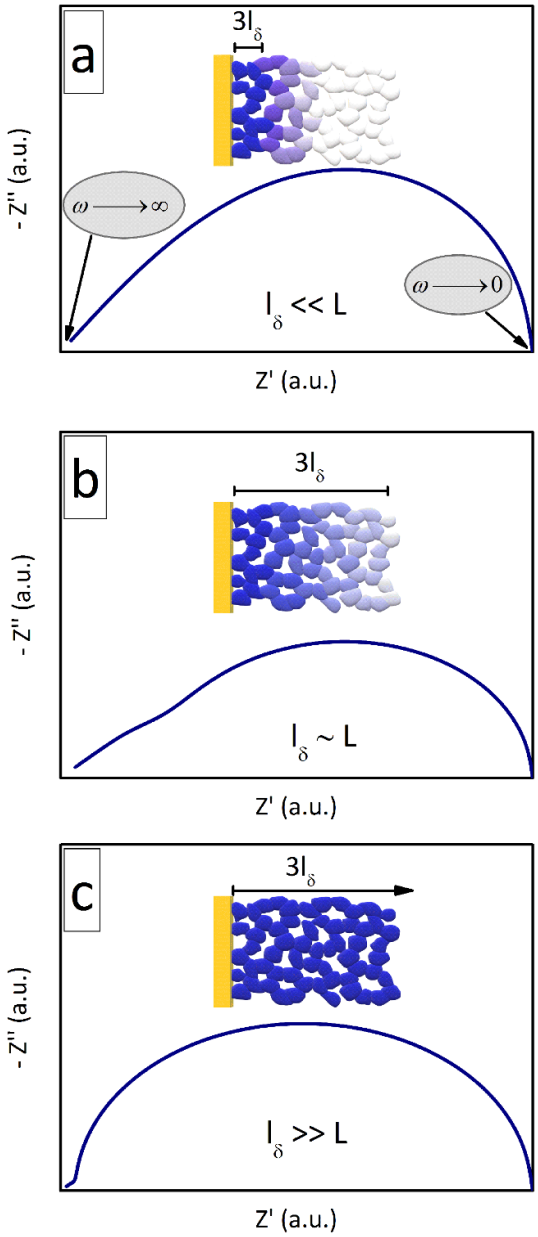

Figure 2. Nyquist representation of TLM circuits in different regimes. (a) semi-infinite condition $L \gg l_\delta$, or $R_d \gg R_s$, the TLM collapses to a Gerischer-type impedance, (b) $L \sim l_\delta$ and (c) $L \ll l_\delta$, or $R_d \ll R_s$, where TLM takes the form of an R//Cpe impedance.

$$l_\delta = L\sqrt{\frac{R_s}{R_d}} \tag{19.3}$$

Furthermore, these relations can also be linked with the phenomenological ALS model to obtain information of the kinetic coefficients in the so-called ALS-TLM model, which models the response of finite-length porous macro-homogeneous electrodes.

Similarly, for the extreme situation when $R_d \ll R_s$, or equivalently $L \ll l_\delta$, the limit $Z_{TLM} \rightarrow Z_{R//Cpe}$ is valid, expressed as:

$$Z_{TLM} = \frac{R_s}{L}\frac{1}{1 + R_s Q_s (j\omega)^\alpha} \tag{20}$$

where $R_s = \frac{RT}{4F^2}\frac{1}{4a\Re_o}$ which can also provide information about k_{chem}, in this condition.

2. Methods

In this work we compare the results obtained from the study of three families of porous electrodes deposited as symmetrical cells on $La_{0.9}Sr_{0.1}Ga_{0.8}Mg_{0.2}O_{2.85}$ (LSGM) or $Ce_{0.9}Gd_{0.1}O_{1.95}$ (GDC) electrolytes: 1. single perovskites with $La_{0.6}Sr_{0.4}Co_{1-x}Fe_xO_{3-\delta}$ composition (with the acronyms LSCF for the family and LSCF6482 meaning x = 0.2 and LSCF6428 meaning x = 0.8); 2. single and double perovskites $La_{0.5-x}Pr_xBa_{0.5}CoO_{3-\delta}$ (LPBC for the family, and x = 0.0, x = 0.20 and x = 0.5); 3. nickelates with Ruddlesden-Popper structure $Nd_2NiO_{4+\delta}$ (NNO).

LSCF and LPBC are non-stoichiometric oxides with O-vacancy defects, whereas NNO can accommodate extra oxygen as O-interstitial defects. All porous electrodes were fabricated following a similar procedure: Powders of electrode materials were synthesized by sol-gel routes, followed by thermal treatments that yielded the desired phases. LSCF (both LSCF6482 and LSCF6428) [57] and one of the NNO electrodes (NNO-SG) [58] were obtained by a chemical method involving a sol-gel formation by polymerization of Acetyl-Acetone (AcAc) and Hexamethylenetetramine (HMTA) [59]. All LPBC electrodes ($x = 0.0$, 0.2 and 0.5) [60] and the second NNO (NNO-P) [61] electrodes were synthesized via a combined EDTA-citrate complexing sol-gel process derived from the Pechini method. In all cases the crystal structures were analysed by x-ray diffraction (XRD), using a Panalytical-Empyrean diffractometer, with Cu K_α radiation.

LSGM and GDC commercial powders (Fuel Cell Materials) were uniaxially pressed and sintered for 6 h at 1450 °C and 1350 °C, respectively, yielding dense electrolytes. LSCF, LPBC and NNO inks were prepared using isopropyl alcohol, alpha-terpineol, polyvinyl butyral, polyvinyl pyrrolidone and LSCF in a weight ratio of 39:24:2:1:34, deposited on the electrolytes using the spin coating technique and calcined at 1000 °C for 1 h. LSCF and NNO electrodes were deposited on LSGM and LPBC on GDC electrolytes.

The microstructural analysis was carried out using 3D FIB-SEM tomography, performed on epoxy infiltrated cells in a FEI Helios Focused Ion Beam—Scanning Electron Microscope (FIB-SEM) using the backscattered electron detector. The images were aligned, filtered and segmented by using a semi-automated algorithm using IMOD [62] and in-house-made Matlab scripts. The image treatment and 3D reconstructions are more thoroughly described in the literature [43, 63]. The porosity ε was calculated by counting the proportion of pore pixels and dividing by the total volume. The surface area a and tortuosity τ values were calculated by using codes written in IDL programming language [64]. Also, the microstructural, structural and compositional characterization was completed, in some cases, by electron microscopy (SEM and TEM), Synchrotron XRD, or inductively coupled plasma-optical emission spectrometry (ICP-OES) studies.

EIS measurements of porous electrodes were carried out using a symmetrical cell configuration. The EIS measurements were performed using a frequency response analyzer coupled to an AUTOLAB potentiostat. EIS spectra were recorded in the temperature range from 500 °C up to 700 °C in dry air. In addition, other EIS measurements were performed at 700 °C as a function of oxygen partial pressure (pO_2) within the range between 10^{-4} to 1 atm., using Ar as the carrier gas. The pO_2 was measured and controlled by using a ZrO_2-based, electrochemical oxygen pump and sensor [65]. For some specific electrodes, these measurements were complemented with similar studies as a function of pO_2, but replacing Ar for He as gas carrier. Finally, for the LPBC electrodes, the study was complemented with the evaluation of the time evolution of the EIS spectra at 700 °C in atmospheric air over 400 h. The EIS spectra were fitted with electrical equivalent circuits using an open source MatLab code [66].

3. Results

3.1. Electrode characterization

XRD provides information about crystal structure (e.g. symmetry, lattice parameters, unit cell volume) and thermogravimetry about defect concentration and how it changes with pO_2, both pieces of information are required for the application of the 3DT-EIS method. Figure 3 shows schematically the crystal structures adopted by LSCF, LPBC and NNO electrodes. In each structure the MO6 (M = Fe, Co, Ni) octahedral unit is indicated. The LSCF compounds present cubic symmetries (S.G. *Pm-3 m,* figure 3(a).) in the whole range of temperatures and pO_2 of this study, with lattice parameters at 700 °C of $a = b = c = 3.8877$ Å and 3.9095 Å for $La_{0.6}Sr_{0.4}Co_{0.8}Fe_{0.2}O_{3-\delta}$ and $La_{0.6}Sr_{0.4}Co_{0.2}Fe_{0.8}O_{3-\delta}$, respectively [67]. LSCF can accommodate O-vacancies in indistinguishable O-sites, thus $x_\delta = \delta/3$ and $x_o = (3-\delta)/3$. At higher Co-content the O-vacancies increase, e.g. $x_\delta = 0.018$ and 0.005 in air at 700 °C for $La_{0.6}Sr_{0.4}Co_{0.8}Fe_{0.2}O_{3-\delta}$ ($3-\delta = 2.946$) and $La_{0.6}Sr_{0.4}Co_{0.2}Fe_{0.8}O_{3-\delta}$ ($3-\delta = 2.985$), respectively [68].

The thermodynamic factor also increases with Co-content (A ~ 4 and 2) [67]. The substitution of Sr by Ba maintains the cubic structure for $La_{0.5}Ba_{0.5}CoO_{3-\delta}$, ($a = b = c = 3.8914$ Å) but the larger ionic radius of Ba^{+2} increases the capability to introduce oxygen vacancies, e.g.: $3-\delta = 2.810$ ($x_\delta = 0.063$) in air at 700 °C

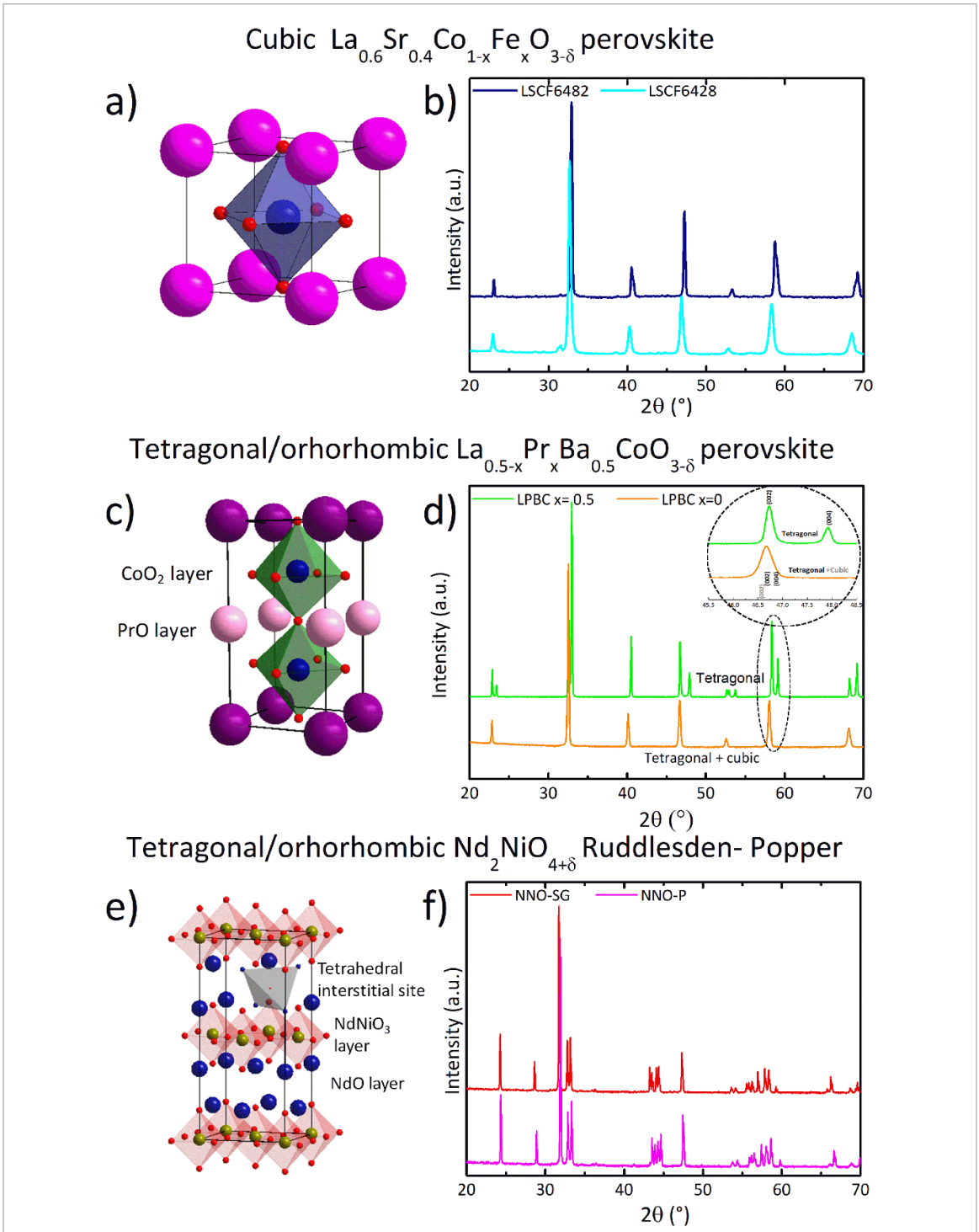

Figure 3. Schemes of crystal structures and powder XRD patterns collected at room temperature of (a)–(b) LSCF cubic *Pm-3 m* perovskite with O-vacancies isotropically distributed in the O-lattice, (c)–(d) tetragonal *P4/mmm* layered double perovskite structure adopted by Pr-rich LPBC. The structure consists of—BaO–CoO_2–PrO–CoO_2–BaO—layers. The O-vacancies are mainly located between PrO and CoO_2 layers. Note at the inset that La-rich LPBC is a mixture of cubic single and tetragonal double perovskites, (e)–(f) orthorhombic *Fmmm* symmetry adopted by the NNO compound with Ruddlesden-Popper structure, consisting of—NdO–$NdNiO_3$–NdO—layers. Extra O-ions can be incorporated in the empty tetrahedral sites generated in the NdO layers. As temperature increases, O-interstitials concentration decreases and NNO adopts a tetragonal I4/mmm structure. This figure remarks one of the eight tetrahedral sites available in this structure. Figure 3(d) [60], figure 3(f) [58].

[69]. As La is replaced by Pr, the difference in the ionic radii of Pr^{+3} and Ba^{+2} promotes the cation ordering in a double perovskite layered structure (figure 3(c)) with tetragonal symmetry and lattice parameters $a = b = 3.9055\ \mathring{A}$ and $c = 7.6319\ \mathring{A}$ [69]. This ordered structure can accommodate more O-vacancies, but these O-vacancies are mainly located in PrO and CoO_2 layers (see figure 3(c)), thus only 5 of 6 oxygen atoms by unit cell are active for O-ion transport and $x_\delta = \delta/2.5$ and $x_o = (2.5 - \delta)/2.5$, e.g.:
$3 - \delta = 2.767$ ($x_\delta = 0.096$) in air at 700 °C for $Pr_{0.5}Ba_{0.5}CoO_{3-\delta}$. The thermodynamic factors of these

compounds are also higher than those of LSCF, presenting values around A ~ 10. Because, as a consequence of the synthesis conditions, La^{3+}/Pr^{3+} and Ba^{2+} cations give place to cationic ordered and disordered structures, the La rich LPBC electrodes presented in this work show a unique microstructure where both, cubic and tetragonal structures, coexist [60].

Other perovskite-related layered structures are the Ruddlesden-Popper phases $A_{n+1}B_nO_{3n+1}$. In these compounds, within every *n* perovskite ABO_3 layers, a rock salt AO intercalated layer can be found. This structure, with n = 1, is adopted by NNO (figure 3(e)). The rock-salt layers generate tetrahedral sites, where the structure can introduce extra O-interstitial sites. Figure 3(e) shows eight tetrahedral sites by unit cell, which include four $Nd_2NiO_{4+\delta}$, thus $x_\delta = \delta/2$ and $x_o = (2-\delta)/2$. According to the amount of extra O-ions, the structure can adopt a tetrahedral or an orthorhombic symmetry. As an example, in air at room temperature the $Nd_2NiO_{4+\delta}$ can accommodate enough ions to make $4+\delta = 4.240$, in an orthorhombic structure (S.G. *Fmmm*), with $a = 5.3769$, b = 5.4509 and c = 12.3647 Å. At 700 °C in air it can accommodate $4+\delta = 4.167$ ($x_\delta = 0.083$) [58, 70] in a tetragonal structure (S.G. *I4mmm*) with a = 3.8630, b = 3.8630 and c = 12.5089 (Å) [19, 71]. The thermodynamic factor in these conditions is A ~ 7. It can be noted that, as temperature increases and pO_2 decreases the materials with O-vacancies increase its number of defects, whereas those with O-interstitials decrease it.

The characterization of the microstructure of the electrode is a key piece of information for the application of the 3DT-EIS method. The left panels of figure 4 show typical 2D sections from FIB-SEM data sets of the porous electrodes, whereas the right panels illustrate the corresponding 3D image representations for (a)–(b) LSCF, (c)–(d) LPBC, (e)–(f) NNO-SG and (g)–(h) NNO-P electrodes. Analysis of the 3D data yields the parameters needed for the application of the ALS model analysis: porosity -ε-, solid phase tortuosity -τ- and specific surface area -*a*-, the latter defined as the cathode area per unit volume. Table 2 lists some characteristic microstructural parameters, obtained from the 3D FIB-SEM reconstructions. In this table, the effect of the synthesis route on the microstructural parameters can be noted by comparing the NNO electrodes. Despite both synthesis methods produce submicronic particles (<500 nm), the formation of denser agglomerates for NNO-P yields a lower specific surface area. In general, those electrodes synthesized by the HMTA-AcAc sol-gel method (LSCF and NNO-SG) exhibit the larger specific surface areas and lower tortuosity values. Also, from comparing LPBC electrodes before and after aging for 400 h in air at 700 °C (see table 2), a reduction of around 15% of the specific surface area is observed. To complement the time-evolution study, the cation surface concentration was measured using ICP-OES [60]. This study indicated that LPBC electrodes present larger amounts of segregated Ba, in the form of $\approx 20\,nm$ sized Ba-rich particles on the perovskite surface. This is especially the case for $Pr_{0.5}Ba_{0.5}CoO_{3-\delta}$, with double perovskite structure, which even just after the preparation of the electrode (before aging) showed a Ba rich surface, that increased about 50% after aging. The other LPBC electrodes increased the estimated amount of segregated BaO monolayers even more after the aging treatment (≈ 100%) [60]. Summarizing, there are two detected changes in the samples before and after aging, one originated in the particle coarsening and the other one associated with the surface cation segregation. However, it is worth noting that the percentage of reduction of specific surface area is significantly lower than the increment in the amount of Ba^{2+} cations on the surface of the electrodes.

3.2. The impedance response

The EIS spectra, collected at 0 V using symmetrical cells with porous electrodes, present different contributions to the total impedances. The analysis of the spectra as a function of pO_2 allows to identify the nature of each contribution according to how the associated polarization resistances vary with pO_2. For example, figure 5 shows selected EIS spectra collected at 700 °C and $pO_2 = 10^{-3}$ atm. for (a) $La_{0.6}Sr_{0.4}Co_{0.8}Fe_{0.2}O_{3-\delta}$ (LSCF6482), (b) $La_{0.3}Pr_{0.2}Ba_{0.5}CoO_{3-\delta}$ (x = 0.2) and (c) $Nd_2NiO_{4+\delta}$ (NNO-SG and NNO-P). One advantage of following the evolution with pO_2 is that at low pO_2 it is easier to see separate arcs. This helps to interpret the arcs at high pO_2 values, where these might be overlapped.

This is the case for LPBC electrodes (figure 5(c)), which exhibit two clear arcs at $pO_2 = 10^{-3}$ atm, one at high frequency (≃500 Hz) and the other at low frequency (≃1 Hz). The low frequency impedance was fitted with an R//Cpe circuit, which corresponds to O_2 gas diffusion according to its dependence with pO_2 ($R_{LF} \propto pO_2^{-1}$) capacitance values (C ≃ 10 F cm^{-2}) and its very low activation energy ($E_a \simeq 0$ eV). Note that at normal ambient pO_2 the gas diffusion resistance contribution is extremely small; the focus here is on the other response that dominates under normal cell operating conditions. This high frequency arc is a Gerischer-type impedance, which is modelled with the ALS approach [60]. The resulting total fits are indicated with solid lines in the figure. For LPBC electrodes, both contributions are clearly distinguishable due to the differences in the characteristic frequencies and the low polarization resistance of the Gerischer-impedance. However, in some cases, the variation of pO_2 is not enough to properly separate overlapped contributions. This is the case of LSCF and NNO electrodes where, despite the Bode plots

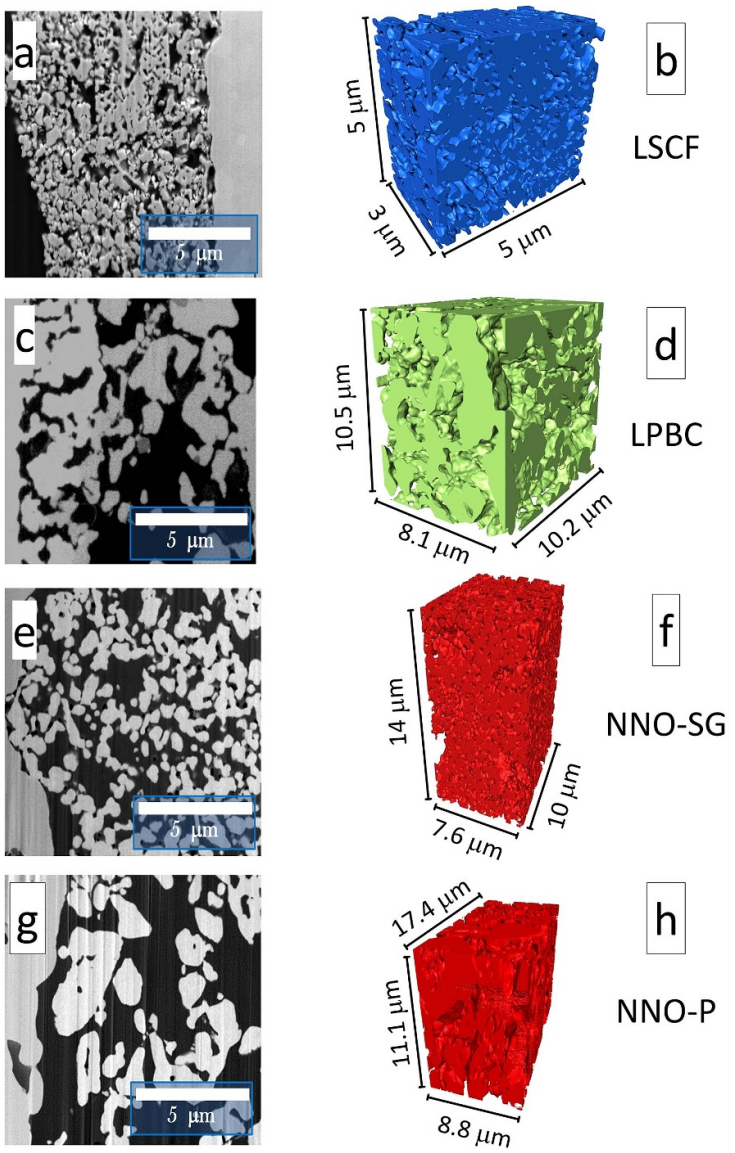

Figure 4. 2D sectional SEM images and 3D image representations of a portion of the reconstructed structures by FIB-SEM tomography (a)–(b) LSCF, (c)–(d) LPBC, (e)–(f) NNO-SG and (g)–(h) NNO-P electrodes. Adapted from [57, 58, 60].

suggesting the presence of two arcs (see LSCF and NNO-P), the shape and size of the arcs is unclear (figures 5(a) and (e)). By changing the gas carrier from Ar to He, the identification of a high frequency TLM element (LSCF electrodes) or Gerischer-type impedance (NNO electrodes), and also a low frequency R//Cpe impedance, was possible. However, when changing from Ar to He, the R//Cpe impedances of the LSCF6428 and NNO-P electrodes do not show the expected reduction, associated with a $\simeq$5 times higher diffusion coefficient of O_2 in He than O_2 in Ar. Then, only for the LSCF6482 electrodes the pure O_2-gas diffusion was identified as a significant contributing process at very low pO_2. On the contrary, in contrast to what was observed for LPBC electrodes, LSCF6428 and NNO-P show a response of the R//Cpe with the typical behaviour of a pure surface process, or a mixed contribution of both surface and O_2 gas diffusion processes [57, 58, 72]. These processes are evidenced by dependencies with pO_2 like $R_{LF} \propto pO_2^{-1/2}$ or $\propto pO_2^{-3/4}$ and lower capacitance values ($C \simeq 0.1$–0.01 F cm^{-2}) than the expected for gas diffusion. Finally, the NNO-SG electrode is fitted in the whole range of pO_2 by using a single Gerischer-type impedance. Figure 5 includes the result of fitting the EIS spectra with these electrical equivalent circuits. The Gerischer-type impedance increases following the trend LPBC < NNO $\approx$ LSCF, for resistances (e.g.: R_G) and time constants as well (e.g.: τ_G). Even though in all cases the dependency with pO_2 is $R_G \propto pO_2^{-1/4}$, a close examination of the slopes of diffusion and surface resistances with pO_2 shows that, in some cases, the $R_G \propto pO_2^{-1/4}$ dependency is only due to the surface process (e.g.: LSCF6482). On the other hand, in other cases it is due to the combination of surface and diffusion resistances (e.g.: LSCF6428) [57]. However, analysing only EIS data, it is unclear if this fact is a consequence of the microstructures or an intrinsic characteristic of the MIEC electrodes, such as its

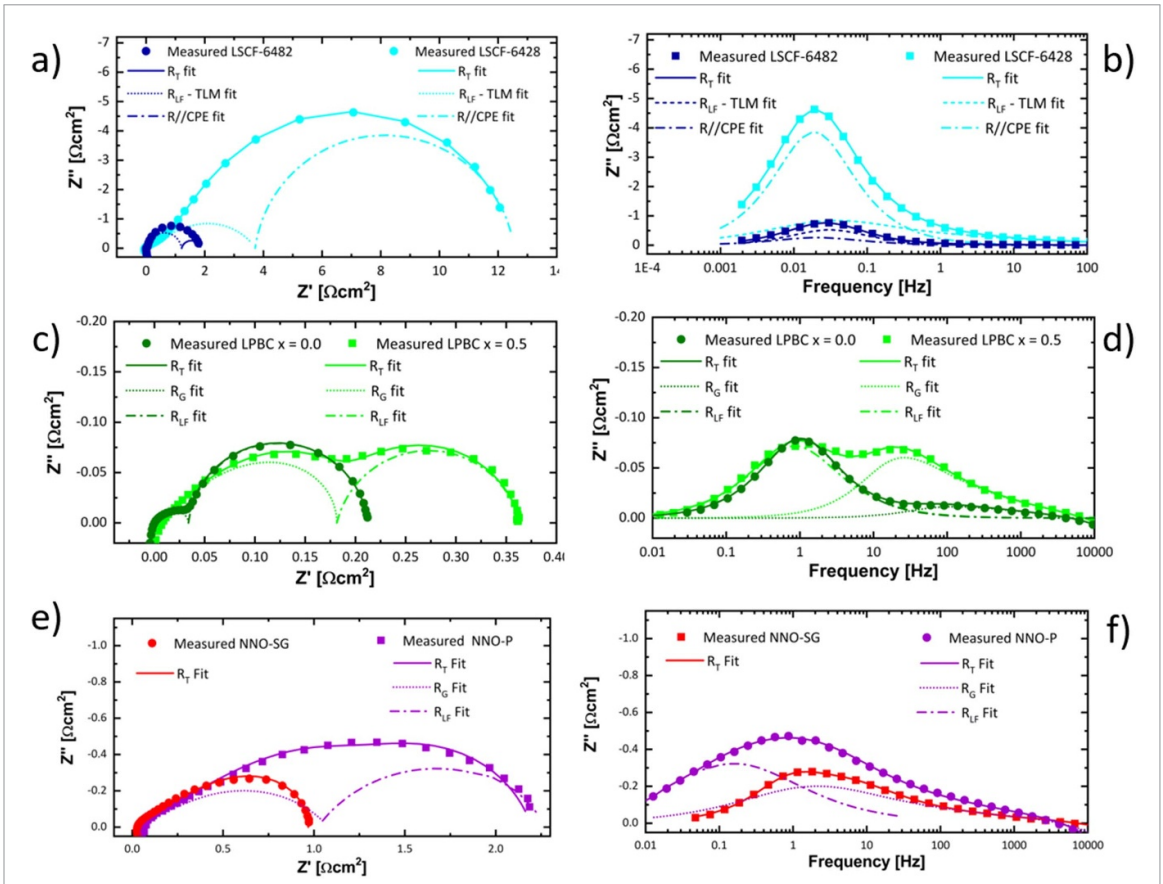

Figure 5. Nyquist and Bode plots of cathodes measured at T = 700 °C and $pO_2 = 10^{-3}$ atm., (a)–(b) LSCF [57], (c)–(d) LPBC [60], (e)–(f) NNO [58, 72]. Symbols correspond to experimental data and lines to the results of fitting.

electrical conductivities, types of O-ion or electronic defects, crystal structures, surface characteristics, etc. In order to help shed light on this key question, in the next section the ALS approach is used to obtain and analyse the kinetic coefficients.

Finally, the evolution with time of the EIS spectra for LPBC electrodes was evaluated with the aim to identify the origin of the electrode degradation. Figures 6(b), (c), (e) and (f) show the EIS spectra, collected at different times, for LPBC ($x = 0.0$ and $x = 0.5$) electrodes. The polarization resistances associated with the contribution of each element are also plotted in figure 6(a) and (d). It is clear that for both electrodes, most of the degradation is in the Gerischer-type impedance (R_G), and that this effect is larger for the double perovskite $Pr_{0.5}Ba_{0.5}CoO_{3-\delta}$ than for the $La_{0.5}Ba_{0.5}CoO_{3-\delta}$ electrode.

3.3. The kinetic coefficients and the ORR limiting mechanisms

The molar surface exchange rate $\Re_o$ and the O-diffusion coefficient D_{chem} were obtained by combining R_G and τ_G, obtained from fitting the EIS spectra, with the microstructural parameters (ε, a and τ) through equations (10.1) and (10.2). The microstructural parameters were extracted from 3D FIB-SEM reconstructions and thermodynamic information of oxygen non-stoichiometry (c_O, x_δ^0 and A). Table 3 compares the values of $\Re_o$ and D_{chem} for all the analysed electrodes in this work, obtained at 700 °C in air. Also, the values of k_{chem} estimated from the relation $\Re_o = k_{chem}\frac{c_\delta}{A}pO_2^n$, or from the relations in equation (2), are included. The pO_2 exponent (n) and the estimated activation energies (E_a) are also listed. The activation energies are calculated from the evolution with temperature (not shown here) [57, 58, 60]. Other literature data, obtained with the same methodology (3DT-EIS) are included for comparison.

With the aim to compare the values of $n = \frac{\partial ln\Re_o}{\partial lnpO_2}$ independently of the absolute values of $\Re_o$, figure 7 shows the normalized molar surface rates $\Re_o/\Re_o(1\,atm)$ for (a) LSCF, (b) LPBC and (c) NNO electrodes, as a function of pO_2 at 700 °C. In these figures, regions where different surface rate mechanisms control the surface reaction are indicated in different grey scales: *chemisorption, dissociative adsorption, dissociation* and *incorporation*. The regions are built by considering different combinations of thermodynamic factors (e.g. A ranging between 2–4 for LSCF electrodes) and different cases for the charge transfer carriers, e.g.: incorporation with ($q_{inc} = 2$) or without ($q_{inc} = 0$) charge transfer.

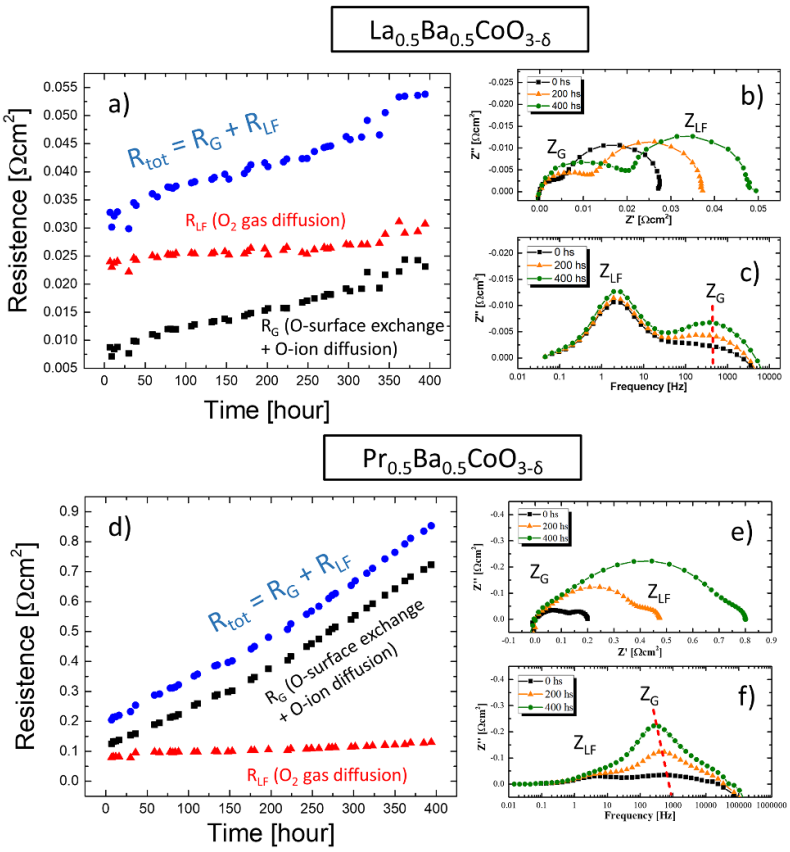

Figure 6. (a) Evolution of total resistance R_{tot}, R_G and R_{LF} values with aging time for $La_{0.5}Ba_{0.5}CoO_{3-\delta}$ electrode at 700 °C in air. Nyquist (b) and Bode (c) plots obtained at 0, 200 and 400 h. (d)–(f) Show the same information for $Pr_{0.5}Ba_{0.5}CoO_{3-\delta}$. Adapted from [60].

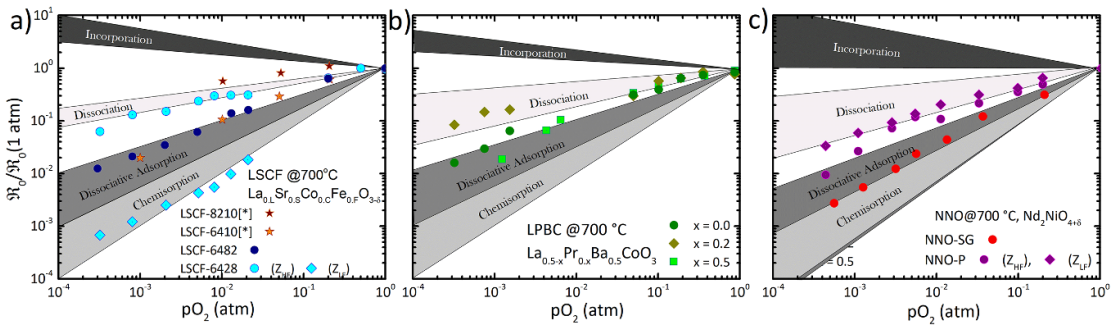

Figure 7. Normalized molar surface rate $\Re_o/\Re_o(1\,atm)$ versus pO_2 at 700 °C for (a) LSCF [57], (b) LPBC [60] and (c) NNO [58] electrodes. Grey regions indicate ranges where surface reaction is *chemisorption, dissociative adsorption, dissociation* or *incorporation*-limited, according to the O-defects involved, thermodynamic factors, metallic or p-type semiconductor or alternative charge transfer amounts obtained by using methodology explained at [51]. [*] correspond to data from Adler's group [29].

For the LSCF6428 and NNO-P electrodes, for which the low frequency impedances -Z_{LF}- were assigned to a surface process (according to its dependencies with pO_2, capacitance values, activation energies, and effect of different gas carriers), its corresponding molar surface exchange rates $\Re_o$ were calculated using equation (20). The normalized molar surface exchange rate values of $La_{0.6}Sr_{0.4}Co_{0.8}Fe_{0.2}O_{3-\delta}$ (LSCF6482) and $La_{0.6}Sr_{0.4}Co_{0.2}Fe_{0.8}O_{3-\delta}$ (LSCF6428) are also compared with $La_{0.8}Sr_{0.2}CoO_{3-\delta}$ (LSCF8210) and $La_{0.6}Sr_{0.4}CoO_{3-\delta}$ (LSCF6410) values, extracted from [29].

Figure 8 shows the chemical diffusion coefficients -D_{chem}- versus pO_2 for (a) LSCF, (b) LPBC and (c) NNO electrodes. The pO_2 dependencies -$m = \frac{\partial lnD_{chem}}{\partial lnpO_2}$- are included in each plot. The D_{chem} values of LSCF6482 and LSCF6428 electrodes are also compared with literature of La-Sr cobaltites data [29].

Figure 9 shows the estimated utilization lengths normalized to the electrode thickness, l_δ/L, as a function of pO_2. The dashed lines correspond to $L = 3l_\delta$, then if $l_\delta/L \gg 1/3$, the finite length electrode approximation

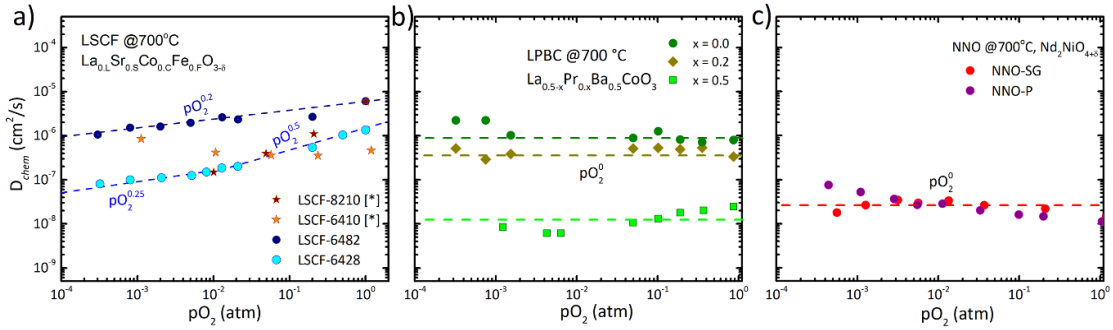

Figure 8. Chemical diffusion coefficients versus pO_2 for (a) LSCF [57], (b) LPBC [60] and (c) NNO [58] electrodes. Dashed lines indicate de dependence with pO_2. [*] correspond to data from Adler's group [29].

is required. That is the case for LSCF electrodes, where the ALS-TLM approach is used to model the electrode response. For the other electrodes, $l_\delta/L < 1/3$ such that the conventional ALD model can be used. The behaviour of l_δ is different for each sample, this is determined by the overall limiting mechanisms of the ORR. For example, at low pO_2 values, the lack of O_2 slows the surface reaction, giving time for O-ions to diffuse from longer distances, hence producing an increase in l_δ/L in all samples as pO_2 decreases. For LPBC ($x = 0.5$) $l_\delta/L \ll 1$, which is consistent with a low diffusion coefficient and high surface exchange rate, as shown in figure 8(b) and table 3. On the contrary, NNO shows similar values of diffusion coefficient to that of LPBC ($x = 0.5$), but the slow surface exchange rate makes the ratio l_δ/L increase, making the reaction to happen all along the electrode. In the case of LSCF, the speed of the surface reaction is slow (see table 3), making all the electrode active.

Finally, the time evolution of the kinetic coefficients for LPBC electrodes is shown in figure 10. The percentage changes are included in the plot. On the one hand, it is notable how the surface exchange coefficient for the double perovskite decreases with time, whereas for the mixed cubic/tetragonal phase k_{chem} did not show significant degradation or even improvement with time. On the other hand, the coefficients associated with O-ion bulk diffusion decrease drastically for all compositions. Figure 10 also includes results from a degradation study performed on a $La_{0.6}Sr_{0.4}Co_{0.2}Fe_{0.8}O_{3-\delta}$ (LSCF6428) commercial electrode [42]. Besides being performed twice as much time as that of the LPBC experiments, the LSCF6428 electrode was also aged at a higher temperature (800 °C) than the LPBC electrodes. Even so, the kinetic parameters of LSCF6428, obtained at 700 °C using the same methodology, show a lower degradation rate.

4. Discussion

In the Results section we showed how the combination of 3D FIB-SEM tomography with EIS and the ALS model can be used to obtain the kinetic parameters of a wide variety of porous MIEC electrodes. The change of $\Re_o/\Re_o\,(1\,atm)$ with pO_2 in figure 7 and the values reported in table 3 are in most cases compatible with a surface rate limiting mechanism controlled by dissociation or dissociative adsorption surface reactions. These surface processes contribute to the Gerischer-type impedance and are co-limiting with the O-diffusion. Figure 8 suggests that, whereas the behaviour of the diffusion coefficients of LPBC and NNO electrodes are consistent with an O-ion bulk path ($D_{chem} \propto pO_2^0$), the dependence of D_{chem} with pO_2 indicates a certain surface character for O-ion diffusion in LSCF electrodes ($D_{chem} \propto pO_2^m$, $m \geq 0.2$). All this information provides the basis for discussing the effect of different structural and chemical properties on the ORR mechanism. Based on these arguments, the rational design of SOFC electrodes becomes a more realistic endeavour. In what follows, we present a brief discussion about the effects of chemical composition, microstructure, and crystallographic structure on the kinetic coefficients and ORR limiting steps.

4.1. Effect of the microstructure on the ORR

The comparison between the $Nd_2NiO_{4+\delta}$ electrodes provides useful information regarding the effect of the microstructure on the kinetic coefficients. These samples were synthesized with different chemical methods, giving as main consequence a three times lower specific surface area for the NNO-P electrodes than for NNO-SG. The diffusion coefficient is not modified in its value or its nature by the change in microstructure. This is expected, considering that the diffusion of the O-ion in NNO is through the bulk of the material, and the change in surface areas, porosity, or tortuosity values should not change the bulk properties of the material.

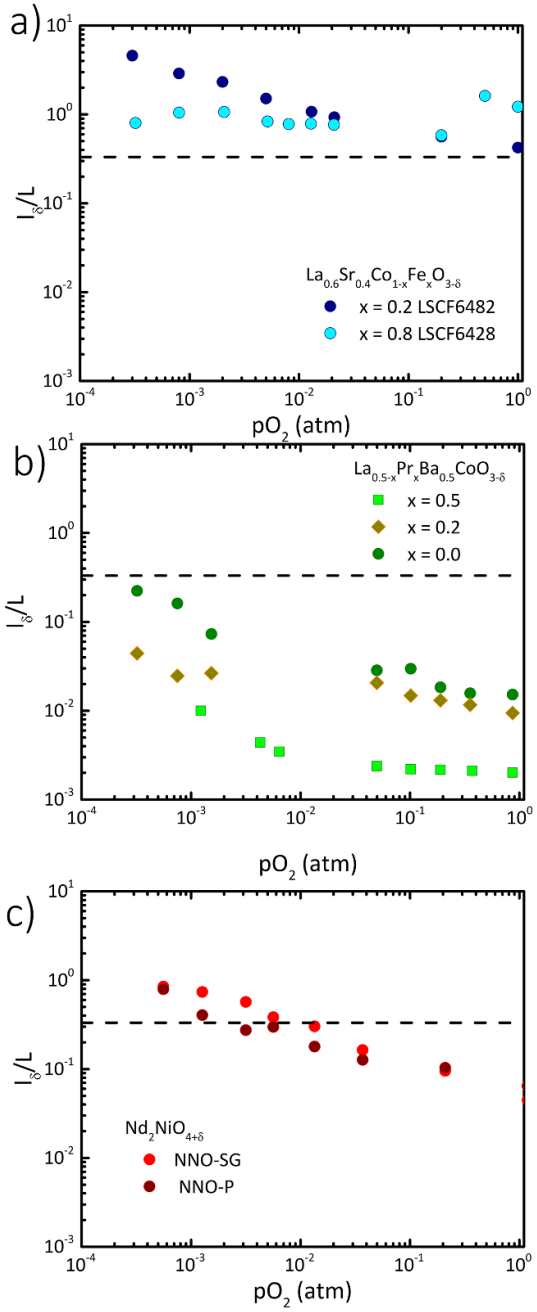

Figure 9. Evolution of utilization length normalized to the electrode thickness, l_δ/L, as a function of pO_2 for (a) $La_{0.6}Sr_{0.4}Co_{1-x}Fe_xO_{3-\delta}$ ($x = 0.2$, LSCF6428 and $x = 0.8$, LSCF6428), (b) $La_{0.5-x}Pr_xBa_{0.5}CoO_{3-\delta}$ (LPBC $x = 0.0$, 0.2 and 0.5) and (c) $Nd_2NiO_{4+\delta}$ synthetized by different routes (NNO-SG and NNO-P). Dashed lines correspond to $L = 3l_\delta$. (a) Adapted from [57], (c) Adapted from [58].

The contribution of surface processes to the impedance is greater for the lower specific surface area NNO-P sample compared to the NNO-SG sample. The main difference observed in the figure 7(c) is the appearance of a new contribution (evidenced by the low frequency impedance arc) for NNO-P. Considering the availability of interstitial sites and the poor electronic conductivity of these nickelates, the O-diffusion is expected to be co-limiting with a surface process involving charge transfer, e.g. O_2-chemisorption. These charge transfer processes have large energy barriers [51, 73], in agreement with those reported in table 3 for NNO electrode (>1.3 eV).

Note that $R_G^{SG} \simeq \frac{\sqrt{a_P}}{\sqrt{a_{SG}}} R_G^P$, in agreement with equation (10.1) and the fact that both electrodes have similar values of molar surface exchange rates (see figure 7 and table 3). This confirms the assumption that the same diffusion and surface processes are associated with the Gerischer response. However, for NNO-P, with a specific surface area three times lower than NNO-SG, a second surface process becomes also rate limiting. Note that in this case $R_{RCpe} \propto \frac{1}{a}$ (see equation (20)) and the impact of changes in specific surface area is higher than in the Gerischer response. This second arc, associated with a surface process, also depends on the

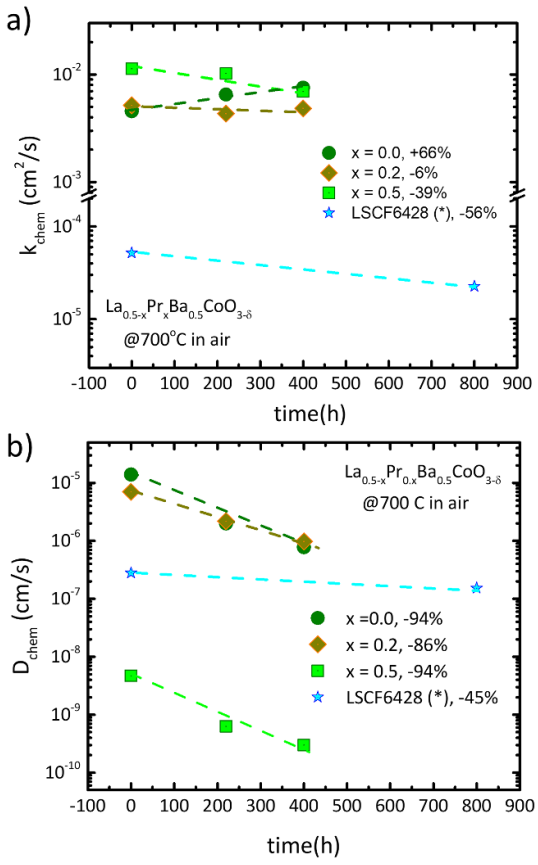

Figure 10. Evolution of kinetic coefficients with time, (a) k_{chem} and (b) D_{chem} for LPBC electrodes evaluated at 700 °C in air [60]. (*) Data corresponding to an LSCF6428 commercial electrode aged at 800 °C and tested at 700 °C is included [42].

feasibility of charge transfer, e.g.: it is dissociation limited. Then, the sequence proposed for the surface exchange reaction could be: $O_2^{gas} \rightarrow O_2^{s} \overset{co-limiting}{\rightarrow} O_2^{-,s} \overset{limiting\,at\,low\,area}{\rightarrow} O^{2-,s}$.

This secondary process in the impedance spectra is relevant only when a low specific surface area limits the availability of active surface sites. However, the possibility of these differences being also due to variations in cation and defect surface concentrations, associated with different processing methods, cannot be discarded. For example, complementary XPS studies indicate that the NNO-P surface is Nd-enriched (Nd^{+3}/Ni^{+2} ratio 70/30) in comparison with the NNO-SG surface (Nd/Ni ratio 55/45). This could be either from Nd-segregation or Ni evaporation during the electrodes processing.

Nevertheless, considering that the surface reaction impacts the resistances as $R_{RCpe} \propto \frac{1}{a}$ or $R_G \propto \frac{1}{\sqrt{a}}$, developing nano-scaled electrodes is one of the main issues in recent SOFC R&D [74, 75]. Particularly, the infiltration of porous ion conductors scaffolds with MIEC oxides gives very low polarization resistances [76, 77], however it also can activate degradation problems associated with particle coarsening processes [7].

4.2. Effect of A-site and B-site substitutions on the reaction mechanism

In this section, the effect of electrode composition is discussed, using the porous electrodes belonging to the single cubic perovskite family of La-Sr cobalt-ferrites as an example. Also for comparison, the La-rich LPBC electrodes are included which, despite having a mixture of cubic and tetragonal phases, present similar characteristics to the cubic perovskites.

The main difference found between these perovskites is in the surface exchange limiting step. The Co-rich compositions, characterized by a metallic band structure (LSCF6482 and LPBC- have electronic conductivities greater than 10^3 S.cm^{-1} [69, 78, 79]) and show O-diffusion convoluted with a dissociative adsorption-limited surface exchange reaction: $O_2^{gas} + s \overset{fast}{\rightarrow} O_2^{-,s} + s \overset{co-limiting}{\rightarrow} 2O^{2-,s}$. For these compounds, the charge is easily transferred from the metallic band, forming an unstable $O_2^{-,s}$ species, then the reaction is limited by the probability of finding an O-vacancy site (s) near the $O_2^{-,s}$ species. This probability is higher for the LPBC electrodes, because they can accommodate more O-vacancies than LSCF6482, which explains the considerably higher surface rates for the La-Ba cobaltites. On the other hand, Fe-rich perovskites, with lower

semiconductor conductivities and lower O-vacancy concentration, seem to have two complementary steps controlling the surface exchange. On the one hand, the O-diffusion is convoluted with O_2-dissociation, which means the ORR is limited by the probabilities of finding a nearby O-vacancy and the energy of transferring charge. On the other hand, the difficulty to transfer charge is also evidenced by the appearance of a secondary surface limiting process as pO_2 decreases, the chemisorption contribution, characterized by a larger time constant: $O_2^{gas} + s \rightarrow O_2^s \overset{limiting\ at\ low\ pO_2}{\rightarrow} O_2^{-,s} + s \overset{co-limiting}{\rightarrow} 2O^{2-,s}$. Generally, reactions limited by charge transfer are characterized by higher activation energies because they have an associated energy barrier, with the addition of the intrinsic large dissociative adsorption negative enthalpy. These kind of differences on the controlling surface mechanism were also reported for $La_{0.6}Sr_{0.4}FeO_{3-\delta}$ (LSF) and $La_{0.6}Sr_{0.4}CoO_{3-\delta}$ (LSC) electrodes [51, 73]. LSF is chemisorption-limited with a high activation energy, whereas LSC is dissociative adsorption-limited, authors also considered that the metallic band structure of LSC helps stabilizing physisorbed O_2 relative to p-type semiconducting LSF.

Differences in the mechanism of O-diffusion are also observed. The O-ion bulk diffusion mechanism acquires a more superficial character for those compositions with lower O-vacancies, e.g.: La-Sr cobalt ferrites seem to have O-diffusion closer to the surface than La-Ba cobaltites. This is evidenced by the increment of the diffusion coefficient dependence with pO_2. These results are similar to those reported by Lu *et al* [29] when comparing $La_{0.6}Sr_{0.4}CoO_{3-\delta}$ with $La_{0.8}Sr_{0.2}CoO_{3-\delta}$ porous electrodes. In short, the O-ion bulk diffusion character decreases following the trend: $La_{0.5}Ba_{0.5}CoO_{3-\delta} \simeq La_{0.6}Sr_{0.4}CoO_{3-\delta} > La_{0.6}Sr_{0.4}Co_{0.8}Fe_{0.2}O_{3-\delta} > La_{0.6}Sr_{0.4}Co_{0.2}Fe_{0.8}O_{3-\delta} > La_{0.8}Sr_{0.2}CoO_{3-\delta}$. The absolute values of the diffusion coefficients (D_{chem}) do not show a clear trend, but in general it takes values between 10^{-6} and 10^{-7} $cm^2.s^{-1}$, where those coefficients associated to an O-ion bulk mechanism show the higher activation energies.

Taking these results into account, it is possible to propose strategies to improve electrode materials according to the origin of the mechanisms controlling both the surface reaction and the O-ion diffusion, without modifying the electrode bulk composition or microstructure. An example following this logic is the surface modification of charge transfer limited materials with high electronic conducting materials, with the aim of assisting the charge transfer reactions. These kind of strategies have already been put into practice in recent years, with promising results, by infiltrating, for example: LSCF6428 cathodes with PrO_x [80, 81], $La_{0.8}Sr_{0.2}MnO_{3-\delta}$ (LSM) [82], Ag nanoparticles and coatings [83]; or Co_3O_4 and Ag particles and coatings into LSF electrodes [84, 85] or amorphous FeO_x coatings on $SrSc_{0.2}Co_{0.8}O_{3-\delta}$ (SSC) [86], among many others. Also, the materials with low oxygen vacancy availability on its surfaces have been modified with ion-conducting materials. An example is the infiltration of LSCF with GDC coatings or nanoparticles [87, 88], where the polarization resistance of a $La_{0.8}Sr_{0.2}Co_{0.5}Fe_{0.5}O_{3-\delta}$ cathode was reduced from 0.65 to 0.2 Ωcm^2, at 700 °C, when it is infiltrated with large amounts of GDC [89]. Similar results were found for a LSCF6428-GDC composite cathode coated with GDC nanoparticles, where the polarization resistance decreases from 0.4 to 0.05 Ωcm^2 at 700 °C with the consequent 20% increment of the SOFC power density [87].

4.3. Effect of A-site substitution on electrode degradation

One of the main issues causing instability of Sr-rich electrodes is Sr-surface segregation [90, 91]. In this section, the effect of composition on the segregation process is considered by comparing the time-dependent response of $La_{0.6}Sr_{0.4}Co_{0.2}Fe_{0.8}O_{3-\delta}$ [42] and $La_{0.5}Ba_{0.5}CoO_{3-\delta}$ [60] porous electrodes.

One of the main differences observed between these two electrodes is the larger Ba-cation surface segregation in comparison with the Sr-segregation: Ba surface concentration increases at approximately twice the rate of the Sr concentration (see [42] and [60]). This is in agreement with the idea proposed in [92] that segregation is linked to the elastic energy generated by the size mismatch at the A site between the host (La) and dopant (Sr^{2+}/Ba^{2+}). Thus, a larger dopant (Ba) tends to segregate faster towards the surface due to the greater amount of elastic energy generated in the system.

The effect of segregation on the kinetic coefficient also varies considerably in the different materials. While Sr-segregation in $La_{0.6}Sr_{0.4}Co_{0.2}Fe_{0.8}O_{3-\delta}$ causes both kinetic parameters to decrease ~50% after aging, for $La_{0.5}Ba_{0.5}CoO_{3-\delta}$ the diffusion coefficient decreases by nearly 100%, but the surface exchange rate actually increases by 66%. In both kinds of electrodes, the surface exchange rates were associated with dissociative adsorption. The extensive literature related to the Sr-segregation problem associates the degradation of the polarization resistance to the fact that the segregation of SrO species blocks the surface exchange process [93]. However, the effect of Ba-segregation is not entirely clear. A few works studying the effect of $BaCO_3$ nanoparticles decorating the surface of LSCF [94] and LSF [95] cathodes demonstrated that Ba ions improve the chemical oxygen surface exchange coefficients, and that the barium ions on the surface might play a key role in the adsorption of oxygen molecules and the formation/decomposition of intermediates [96]. This

could be the case of $La_{0.5}Ba_{0.5}CoO_{3-\delta}$, where the formation of Ba-rich nanoparticles on the surface of the aged electrode was observed.

The degradation of D_{chem} deserves a separate consideration because the pO_2 dependence suggested an O-ion bulk diffusion mechanism. Then, it is reasonable to assume that this decrease would be associated with a negative impact of the Ba/Sr depletion in the sub-surface region, which naturally accompanies the cation-surface enrichment during segregation. It is plausible that the loss of Ba/Sr could produce a local lattice distortion affecting the O-ion transport, affecting the surface diffusion processes.

The Ba/Sr segregation may be controlled or reduced, for example, the Sr segregation on LSCF decreases substantially by reducing the operation temperature [42, 97]. Also, taking into account that the cation segregation is promoted by the increase in elastic energy due to the size mismatch at the A-site, a simpler alternative would be to reduce the elastic energy by specifically doping with smaller cations -e.g.: partial substitution of Sr^{2+} by Ca^{2+}, or Ba^{2+} by Sr^{2+} in La-Sr and La-Ba cobaltites, respectively- or by generating free space in A-site deficient materials. However, both cation substitution and A site-deficiency also modify the kinetic parameters. Another alternative could be to prevent the Ba/Sr segregation by decorating the surface. This decoration could either modify the local elastic energy or the electroneutrality of the surface to prevent cation segregation. For example, the stable operation of $La_{0.6}Sr_{0.4}Co_{0.2}Fe_{0.8}O_{3-\delta}$ electrodes after aging was assigned to the suppression of SrO segregation by a surface decoration with GDC nano-particles [98]. Cation surface segregation is also promoted by the increase of surface oxygen vacancy concentration and, for this reason, an alternative to suppress this effect is covering the surface with less reducible cations such as Hf or Zr [99]. More details about this kind of strategies to mitigate Sr and Ba segregation can be found in [91].

4.4. Effect of crystal structure on the reaction mechanism

To analyze the effect of crystal structure on the mechanism of reaction, the results of the layered electrodes (Pr-rich LPBC and NNO) are compared with those of single cubic perovskite electrodes (La-rich LPBC and LSCF). In general, the main effect of the structuring of perovskites in layered structures is to reduce the diffusion coefficients. Thus, cubic perovskites present higher diffusion coefficients than layered nickelates—with interstitial O-ion conduction -, which in turn present larger diffusion coefficients than layered perovskites with O-vacancy conduction mechanisms.

Unlike LSCF and LPBC electrodes, NNO electrodes have O-interstitials instead of O-vacancies. These kind of defects are highly mobile [100], but it has been theoretically [101] and experimentally [102] demonstrated that in these nickelates the O-ion diffusion is highly anisotropic through the a–b plane in NdO layers (see figure 3(e)). Thus, although the mobility of O-interstitials is high, it is reasonable to assume that the lower O-diffusion coefficient for NNO than for isotropic cubic perovskite structures must be a consequence of a 2D diffusion path for O-migration.

On the other hand, theoretical [101, 103, 104] and experimental [79] studies also confirm the anisotropic oxygen diffusion in layered Ln–Ba–Co–O structures, characterized by migration from the Ln–O layer to the Co–O layer or vice versa. This anisotropic migration reduces the ionic conductivity for tetragonal $PrBaCo_2O_{6-\delta}$ [69] and the polarization resistance of $LaBaCo_2O_{6-\delta}$ cathodes [10] respect to those of cubic $La_{0.5}Ba_{0.5}CoO_{3-\delta}$ perovskites. However, the difference between the tetragonal perovskites studied in [10, 69] and the La-rich LPBC presented in this work, is that the latter are a mixture of cubic and tetragonal phases. This phase mixture could be the cause of the improvement in the ORR polarization resistance, as it was proposed for two-phases composites prepared by mixing different order Ruddlesden-Popper nickelates [105]. However, neither the simple mixture of two phases or the isotropic diffusion for cubic perovskites can explain the two orders of magnitude difference in D_{chem} between the pure tetragonal Pr-rich LPBC ($D_{chem} \simeq 10^{-8}$ $cm^2.s^{-1}$) and the cubic-mixed-with-tetragonal La-rich electrodes ($D_{chem} \simeq 10^{-6}$ $cm^2.s^{-1}$) discussed here. The reason for this difference seems to be related to the fact that La-rich LPBC electrodes are not a regular composite resulting from a simple phase mixture. These electrodes show a unique microstructure, where the cubic and tetragonal phases coexist intimately mixed (see figure 3(d)), forming heterostructured interphases. This microstructure is highly distorted, with highly defective interfaces that can promote fast O-grain boundary diffusion as it was proposed to happen for a $La_{0.3}Pr_{0.2}Ba_{0.5}CoO_{3-\delta}$ dense membrane with highly distorted structure, which showed an ionic conductivity one order of magnitude higher than pure cubic and tetragonal phases [69].

This kind of anomalous behaviour in the ORR has already been reported in the case of a specially designed heterostructure, with LSC-113/214 interfaces, formed by $La_{1-x}Sr_xCoO_{3-\delta}$ (LSC-113) and the Ruddlesden-Popper $(La_{0.5}Sr_{0.5})_2CoO_{4-}$(LSC-214) phases [106–109]. These studies consistently show that, when compared to bulk or thin LSC-113 or LSC-214 films, the LSC-113/214 heterointerfaces dramatically enhance the oxygen exchange rate and ORR kinetics. The authors explained this improvement through an A-site cation interdiffusion across the LSC-113/214 interface, which leads to the increase in the O-vacancy concentration enhancing the interfacial conductivity, surface oxygen exchange and therefore the ORR

kinetics [110]. Thus, a similar situation could be expected for La-rich LPBC electrodes, where the presence of highly active interfaces could explain the two orders of magnitude higher diffusion coefficient. This opens a door for new design ideas for SOFC electrodes including complex heterointerfaces.

4.5. Effect of crystal structure on electrode degradation

Figure 10 shows that time evolution affects both, the diffusion coefficient and the surface exchange rate for LPBC electrodes. In all cases, the O-ion bulk diffusion decreases around 100% independently of the structural effect discussed in the previous section. On the other hand, although the mechanism of surface reaction is the same for all LPBC electrodes, the value of k_{chem} is noticeably higher for the layered structures than for other electrodes (See table 3). Also a different evolution with time behavior is observed for tetragonal perovskite e.g.: k_{chem} decreases with time for Pr-rich LPBC electrodes while it increases or stays almost constant for La-rich LPBC electrodes (figure 10). From the analysis of the time evolution of the polarization resistance (figure 6), microstructure and surface cation concentration, it was concluded that degradation is mainly due to the Ba-surface segregation (increases about 50%–100% during aging) rather than particle coarsening (reduce specific surface about 15%) [60].

Note that Ba-segregation is so fast that it also takes place during the sample processing. However, the Ba segregation is especially high for the tetragonal phase ($Pr_{0.5}Ba_{0.5}CoO_{3-\delta}$), where the estimated number of monolayers in the as-prepared electrodes is more than twice as much as the observed for the other LPBC electrodes and, as with other electrodes, also increases with time [60]. It has also been argued that Ba-segregation probably has an active role in two competing processes; on the one hand it seems to play a positive role in the formation/decomposition of intermediates for O_2 adsorption [96], whereas on the other hand it can block the surface exchange process [93], in a similar fashion to what is observed with Sr segregation.

Considering that the tetragonal phase (LPBC $x = 0.5$) has the higher Ba-surface concentration and the higher initial k_{chem}, the highly negative impact in the surface exchange rate observed is expected to be due to the -almost complete- blocking of surface sites for reaction. But for the La-rich LPBC electrodes with lower surface exchange rate, the low Ba-surface concentration can either have a neutral effect or even improve the surface reaction, by assisting in the dissociative adsorption through the promotion of the O-vacancies formation. However, in all cases, the global impact of Ba-segregation is detrimental to the response of the electrode and, as discussed above, the implementation of strategies to avoid cation surface segregation are strongly recommended.

5. Conclusions

In this review, the 3DT-EIS method for obtaining the ORR kinetic parameters (k_{chem} and D_{chem}) for porous MIEC materials, with applications to SOFC electrodes and other energy devices is discussed. This method combines EIS and 3D FIB-SEM tomography measurements with analysis done using the ALS model. Besides the understanding of the basic mechanisms controlling the responses of the electrodes, the 3DT-EIS method allows the identification of specific effects produced by differences in nano/microstructure, surface compositions, crystal structure and A or B specific doping effects on the kinetic parameters of real porous electrodes. This method has advantages compared with other experimental techniques, including the ability to measure both k and D over a wide range of conditions, and obtaining quantities that are relevant to actual electrodes prepared under normal processing conditions. Also note that the increasing availability of 3D FIB-SEM tomography, in combination with the widely-used EIS measurements, makes this experimental approach more readily accessible, such that a more widespread use is expected to be seen in the near future.

For the discussion, results of La-Sr cobalt ferrites ($La_{0.6}Sr_{0.4}Co_{1-x}Fe_xO_{3-\delta}$, $x = 0.2$ and 0.8), La/Pr-Ba cobaltites ($La_{0.5-x}Pr_xBa_{0.5}CoO_{3-\delta}$, $x = 0.0$, 0.2 and 0.5) and Ruddlesden-Popper nickelates ($Nd_2NiO_{4+\delta}$) were shown as specific examples about the effect of the chemical composition, crystal structure, and microstructure on the ORR and electrode degradation mechanisms.

The analysis of the dependence of molar surface exchange rates with oxygen partial pressure provides information about the mechanisms limiting the O_2-surface reaction. According to the interplay between electronic conductivity and availability of surface empty sites, two alternative surface reaction paths were observed: *dissociative-adsorption*, limited by the availability of near empty surface sites $O_2^{gas} \rightarrow O_2^{-,s} \overset{limiting}{\rightarrow} O^{2-,s}$ or *chemisorption* followed by *dissociation*, both limited by the probability of charge transfer $O_2^{gas} + s \rightarrow O_2^{s} \overset{limiting}{\rightarrow} O_2^{-,s} + s \overset{limiting}{\rightarrow} 2O^{2-,s}$.

At 700 °C in air, the highest values of k_{chem} correspond to the La-Ba cobaltite structures ($La_{0.5-x}Pr_xBa_{0.5}CoO_{3-\delta}$), showing a value of $k_{chem} \simeq 0.5$–$1\ 10^{-2}$ cm.s^{-1}. Two orders of magnitude lower values were observed for the nickelate $Nd_2NiO_{4+\delta}$ and the La-Sr cobalt ferrites ($k_{chem} \simeq 1$–$5\ 10^{-5}$ cm.s^{-1}).

On the contrary, the diffusion coefficients D_{chem} are higher for cubic perovskites than for the layered ones. For $La_{0.6}Sr_{0.4}Co_{0.8}Fe_{0.2}O_{3-\delta}$ and $La_{0.6}Sr_{0.4}Co_{0.2}Fe_{0.8}O_{3-\delta}$, D_{chem} is 2.6 10^{-6} and 5.4 10^{-7} $cm^2.s^{-1}$, respectively. These values are comparable to the D_{chem} value of 1.2 10^{-6} $cm^2.s^{-1}$ observed for $La_{0.5}Ba_{0.5}CoO_{3-\delta}$. However, whereas the large O-vacancy content allows for an O-ion bulk diffusion mechanism for La/Pr-Ba cobaltites, as Fe content increases in La-Sr cobalt ferrites, the surface character of O-ion diffusion also increases. The layered structure drastically reduces the O-ion bulk diffusion due to anisotropy effects, e.g.: $D_{chem} = 1.3$ 10^{-8} $cm^2.s^{-1}$ for the $Pr_{0.5}Ba_{0.5}CoO_{3-\delta}$ double perovskite. However, in the case of $Nd_2NiO_{4+\delta}$, this effect is compensated by a high mobility of O-interstitials ($D_{chem} \simeq 10^{-7} cm^2.s^{-1}$).

Analysis of the time evolution of the electrodes shows that surface cation segregation affects both the O-ion bulk diffusion and the surface exchange rates. Although the impact of the cation surface segregation on the diffusion coefficient is negative in all cases—e.g.: diffusion coefficients are reduced 100% for both La-Sr and La-Ba single and double layer perovskites—the surface exchange rate can be impacted either negatively or positively. This depends on the competition between two possible effects, the ORR surface sites blocking by Sr/Ba- segregation or the dissociative adsorption assistance by BaO nanoparticles.

Finally, some strategies to reduce the cathode polarization losses are discussed, with specific examples and proposals for materials design strategies.

Acknowledgments

The authors at Centro Atómico Bariloche acknowledge the financial support of Comisión Nacional de Energía Atómica (CNEA), Consejo Nacional de Investigaciones Científicas y Técnicas (CONICET), Agencia Nacional de Promoción de Ciencia y Tecnología (ANPCyT PICT 2016-2965) and Instituto Balseiro-Universidad Nacional de Cuyo. The authors at Northwestern gratefully acknowledge financial support from the US National Science Foundation grant DMR-1912530. The authors also acknowledge the Fulbright Program.

ORCID iDs

Julián Ascolani-Yael https://orcid.org/0000-0003-0776-2393
Alejandra Montenegro-Hernández https://orcid.org/0000-0002-0816-278X
Diana Garcés https://orcid.org/0000-0001-5623-4621
Quinyuan Liu https://orcid.org/0000-0002-8805-1587
Scott Barnett https://orcid.org/0000-0001-9813-7360
Liliana Mogni https://orcid.org/0000-0002-4665-9439

References

[1] Jiang S P 2019 Development of lanthanum strontium cobalt ferrite perovskite electrodes of solid oxide fuel cells—a review *Int. J. Hydrog. Energy* **44** 7448–93
[2] Wang W G and Mogensen M 2005 High-performance lanthanum-ferrite-based cathode for SOFC *Solid State Ionics* **176** 457–62
[3] Tietz F, Haanappel V A C, Mai A, Mertens J and St D 2006 Performance of LSCF cathodes in cell tests *J. Power Sources* **156** 20–22
[4] Leonide A, Rüger B, Weber A, Meulenberg W A and Ivers-Tiffée E 2010 Impedance study of alternative $(La,Sr)FeO_{3-\delta}$ and $(La,Sr)(Co,Fe)O_{3-\delta}$ MIEC cathode compositions *J. Electrochem. Soc.* **157** B234
[5] Grunbaum N, Dessemond L, Fouletier J, Prado F, Mogni L and Caneiro A 2009 Rate limiting steps of the porous $La_{0.6}Sr_{0.4}Co_{0.8}Fe_{0.2}O_{3-\delta}$ electrode material *Solid State Ion.* **180** 1448–52
[6] Baqué L C, Soldati A L, Teixeira-Neto E, Troiani H E, Schreiber A and Serquis A C 2017 Degradation of oxygen reduction reaction kinetics in porous $La_{0.6}Sr_{0.4}Co_{0.2}Fe_{0.8}O_{3-\delta}$ cathodes due to aging-induced changes in surface chemistry *J. Power Sources* **337** 166–72
[7] Shah M, Voorhees P W and Barnett S A 2011 Time-dependent performance changes in LSCF-infiltrated SOFC cathodes: the role of nano-particle coarsening *Solid State Ion.* **187** 64–67
[8] Tarancon A, Penamartinez J, Marrerolopez D, Morata A, Ruizmorales J and Nunez P 2008 Stability, chemical compatibility and electrochemical performance of $GdBaCo_2O_{5+x}$ layered perovskite as a cathode for intermediate temperature solid oxide fuel cells *Solid State Ion.* **179** 2372–8
[9] Kim G, Wang S, Jacobson A J, Reimus L, Brodersen P and Mims C A 2007 Rapid oxygen ion diffusion and surface exchange kinetics in $PrBaCo_2O_{5+x}$ with a perovskite related structure and ordered A cations *J. Mater. Chem.* **17** 2500
[10] Garcés D, Soldati A L, Troiani H, Montenegro-Hernández A, Caneiro A and Mogni L V 2016 La/Ba-based cobaltites as IT-SOFC cathodes: a discussion about the effect of crystal structure and microstructure on the O_2-reduction reaction *Electrochim. Acta* **215** 637–46
[11] Zhang K, Ge L, Ran R, Shao Z and Liu S 2008 Synthesis, characterization and evaluation of cation-ordered $LnBaCo_2O_{5+\delta}$ as materials of oxygen permeation membranes and cathodes of SOFCs *Acta Mater.* **56** 4876–89
[12] Tarancón A, Morata A, Dezanneau G, Skinner S J, Kilner J A, Estradé S, Hernández-Ramírez F, Peiró F and Morante J R 2007 $GdBaCo_2O_{5+x}$ layered perovskite as an intermediate temperature solid oxide fuel cell cathode *J. Power Sources* **174** 255–63
[13] Kim J-H, Mogni L, Prado F, Caneiro A, Alonso J A and Manthiram A 2009 High temperature crystal chemistry and oxygen permeation properties of the mixed ionic–electronic conductors $LnBaCo_2O_{5+\delta}$ (Ln=Lanthanide) *J. Electrochem. Soc.* **156** B1376

[14] Zhou Q, He T and Ji Y 2008 $SmBaCo_2O_{5+x}$ double-perovskite structure cathode material for intermediate-temperature solid-oxide fuel cells *J. Power Sources* **185** 754–8

[15] Zhou Q, Wang F, Shen Y and He T 2010 Performances of $LnBaCo_2O_{5+x}$-$Ce_{0.8}Sm_{0.2}O_{1.9}$ composite cathodes for intermediate-temperature solid oxide fuel cells *J. Power Sources* **195** 2174–81

[16] Merkle R, Mastrikov Y A, Kotomin E A, Kuklja M M and Maier J 2012 First principles calculations of oxygen vacancy formation and migration in $Ba_{1-x}Sr_xCo_{1-y}Fe_yO_{3-\delta}$ perovskites *J. Electrochem. Soc.* **159** B219

[17] Pikalov S M, Vedmid L B, Filonova E A, Pikalova E Y, Lyagaeva J G, Danilov N A and Murashkina A A 2019 High-temperature behavior of calcium substituted layered neodymium nickelates *J. Alloys Compd.* **801** 558–67

[18] Wang J Q, Zhou D F, Gao J Q, Sun H R, Zhu X F and Meng J 2018 Effect of A/B-Site Non-stoichiometry on the structure and properties of $La_{0.9}Sr_{0.1}Ga_{0.9}Mg_{0.1}O_{3-\delta}$ solid electrolyte in intermediate-temperature solid oxide fuel cells *Chem. Electro. Chem.* **5** 665–73

[19] Montenegro-Hernández A, Vega-Castillo J E, Caneiro A and Mogni L 2020 Effects of neodymium doping on oxygen reduction activity in $Pr_{2-x}Nd_xNiO_{4+\delta}$ cathodes *Solid State Ion.* **347**

[20] Kilner J A, Skinner S J and Brongersma H H 2011 The isotope exchange depth profiling (IEDP) technique using SIMS and LEIS *J. Solid State Electrochem.* **15** 861–76

[21] Armstrong E N, Duncan K L, Oh D J, Weaver J F and Wachsman E D 2011 Determination of surface exchange coefficients of LSM, LSCF, YSZ, GDC constituent materials in composite SOFC cathodes *J. Electrochem. Soc.* **158** B492

[22] Wang L, Merkle R and Maier J 2010 Surface kinetics and mechanism of oxygen incorporation into $Ba_{1-x}Sr_xCo_yFe_{1-y}O_{3-\delta}$ SOFC microelectrodes *J. Electrochem. Soc.* **157** B1802

[23] Lane J A and Kilner J A 2000 Measuring oxygen diffusion and oxygen surface exchange by conductivity relaxation *Solid State Ion.* **136–7** 997–1001

[24] Li Y, Gerdes K, Horita T and Liu X 2013 Surface exchange and bulk diffusivity of LSCF as SOFC cathode: electrical conductivity relaxation and isotope exchange characterizations *J. Electrochem. Soc.* **160** F343–50

[25] Preis W, Bucher E and Sitte W 2002 Oxygen exchange measurements on perovskites as cathode materials for solid oxide fuel cells *J. Power Sources* **106** 116–21

[26] Cox-Galhotra R A and McIntosh S 2010 Unreliability of simultaneously determining kchem and Dchem via conductivity relaxation for surface-modified $La_{0.6}Sr_{0.4}Co_{0.2}Fe_{0.8}O_{3-\delta}$ *Solid State Ion.* **181** 1429–36

[27] Riva M *et al* 2018 Influence of surface atomic structure demonstrated on oxygen incorporation mechanism at a model perovskite oxide *Nat. Commun.* **9** 3710

[28] Søgaard M, Hendriksen P V, Mogensen M, Poulsen F W and Skou E 2006 Oxygen nonstoichiometry and transport properties of strontium substituted lanthanum cobaltite *Solid State Ion.* **177** 3285–96

[29] Lu Y, Kreller C and Adler S B 2009 Measurement and modeling of the impedance characteristics of porous $La_{1-x}Sr_xCoO_{3-\delta}$ electrodes *J. Electrochem. Soc.* **156** B513

[30] Adler S, Lane J and Steele B 1996 Electrode kinetics of porous mixed-conducting oxygen electrodes *J. Electrochem.* **143** 3554–64

[31] Adler S B 1998 Mechanism and kinetics of oxygen reduction on porous $La_{1-x}Sr_xCoO_{3-\delta}$ electrodes *Solid State Ion.* **111** 125–34

[32] Wilson J R, Kobsiriphat W, Mendoza R, Chen H-Y, Hiller J M, Miller D J, Thornton K, Voorhees P W, Adler S B and Barnett S A 2006 Three-dimensional reconstruction of a solid-oxide fuel-cell anode *Nat. Mater.* **5** 541–4

[33] Cocco A P, Nelson G J, Harris W M, Nakajo A, Myles T D, Kiss A M, Lombardo J J and Chiu W K S 2013 Three-dimensional microstructural imaging methods for energy materials *Phys. Chem. Chem. Phys.* **15** 16377

[34] Joos J, Ender M, Carraro T, Weber A and Ivers-Tiffée E 2012 Representative volume element size for accurate solid oxide fuel cell cathode reconstructions from focused ion beam tomography data *Electrochim. Acta* **82** 268–76

[35] Möbus G and Inkson B J 2007 Nanoscale tomography in materials science *Mater. Today* **10** 18–25

[36] Dierickx S, Joos J, Weber A and Ivers-Tiffée E 2018 Advanced impedance modelling of Ni/YSZ cermet anodes *Electrochim. Acta* **265** 736–50

[37] Holzer L *et al* 2011 Microstructure degradation of cermet anodes for solid oxide fuel cells: quantification of nickel grain growth in dry and in humid atmospheres *J. Power Sources* **196** 1279–94

[38] Bertei A, Ruiz-Trejo E, Tariq F, Yufit V, Atkinson A and Brandon N P 2016 Validation of a physically-based solid oxide fuel cell anode model combining 3D tomography and impedance spectroscopy *Int. J. Hydrog. Energy* **41** 22381–93

[39] Zhang Y, Yan F, Yan M, Wan Y, Jiao Z, Xia C, Chen F and Ni M 2019 High-throughput, super-resolution 3D reconstruction of nano-structured solid oxide fuel cell electrodes and quantification of microstructure-property relationships *J. Power Sources* **427** 112–9

[40] Dierickx S, Mundloch T, Weber A and Ivers-Tiffée E 2019 Advanced impedance model for double-layered solid oxide fuel cell cermet anodes *J. Power Sources* **415** 69–82

[41] Almar L, Szász J, Weber A and Ivers-Tiffée E 2017 Oxygen transport kinetics of mixed ionic-electronic conductors by coupling focused ion beam tomography and electrochemical impedance spectroscopy *J. Electrochem. Soc.* **164** F289–97

[42] Wang H, Yakal-Kremski K J, Yeh T, Rupp G M, Limbeck A, Fleig J and Barnett S A 2016 Mechanisms of performance degradation of $(La,Sr)(Co,Fe)O_{3-\delta}$ solid oxide fuel cell cathodes *J. Electrochem. Soc.* **163** F581–5

[43] Scott Cronin J, Muangnapoh K, Patterson Z, Yakal-Kremski K J, Dravid V P and Barnett S A 2012 Effect of firing temperature on LSM-YSZ composite cathodes: a combined three-dimensional microstructure and impedance spectroscopy study *J. Electrochem. Soc.* **159** B385–93

[44] Marinha D, Dessemond L, Cronin J S, Wilson J R, Barnett S A and Djurado E 2011 Microstructural 3D reconstruction and performance evaluation of LSCF cathodes obtained by electrostatic spray deposition *Chem. Mater.* **23** 5340–8

[45] Wilson J R, Cronin J S and Barnett S A 2011 Linking the microstructure, performance and durability of Ni-yttria-stabilized zirconia solid oxide fuel cell anodes using three-dimensional focused ion beam–scanning electron microscopy imaging *Scr. Mater.* **65** 67–72

[46] Gostovic D, Smith J R, Kundinger D P, Jones K S and Wachsman E D 2007 Three-dimensional reconstruction of porous LSCF cathodes *Electrochem. Solid-State Lett.* **10** B214

[47] Gostovic D, Vito N J, O'Hara K A, Jones K S and Wachsman E D 2011 Microstructure and connectivity quantification of complex composite solid oxide fuel cell electrode three-dimensional networks *J. Am. Ceram. Soc.* **94** 620–7

[48] Ni N, Cooper S J, Williams R, Kemen N, McComb D W and Skinner S J 2016 Degradation of $(La_{0.6}Sr_{0.4})_{0.95}(Co_{0.2}Fe_{0.8})O_{3-\delta}$ solid oxide fuel cell cathodes at the nanometer scale and below *ACS Appl. Mater. Interfaces* **8** 17360–70

[49] Lu M Y, Railsback J G, Wang H, Liu Q, Chart Y A, Zhang S L and Barnett S A 2019 Stable high current density operation of $La_{0.6}Sr_{0.4}Co_{0.2}Fe_{0.8}O_{3-\delta}$ oxygen electrodes *J. Mater. Chem.* A **7** 13531–9

[50] Druce J, Téllez H, Burriel M, Sharp M D, Fawcett L J, Cook S N, McPhail D S, Ishihara T, Brongersma H H and Kilner J A 2014 Surface termination and subsurface restructuring of perovskite-based solid oxide electrode materials *Energy Environ. Sci.* **7** 3593–9

[51] Adler S B, Chen X Y and Wilson J R 2007 Mechanisms and rate laws for oxygen exchange on mixed-conducting oxide surfaces *J. Catal.* **245** 91–109

[52] Lankhorst M H R, Bouwmeester H J M and Verweij H 2005 Thermodynamics and transport of ionic and electronic defects in crystalline oxides *J. Am. Ceram. Soc.* **80** 2175–98

[53] Lankhorst M H R, Bouwmeester H J M and Verweij H 1996 Use of the rigid band formalism to interpret the relationship between O chemical potential *Phys. Rev. Lett.* 2989–92

[54] Lankhorst M H R, Bouwmeester H J M and Verweij H 1997 High-temperature coulometric titration of $La_{1-x}Sr_xCoO_{3-\delta}$: evidence for the effect of electronic band structure on nonstoichiometry behavior *J. Solid State Chem.* **133** 555–67

[55] Nielsen J, Hjalmarsson P, Hansen M H and Blennow P 2014 Effect of low temperature in-situ sintering on the impedance and the performance of intermediate temperature solid oxide fuel cell cathodes *J. Power Sources* **245** 418–28

[56] Hjalmarsson P, Søgaard M and Mogensen M 2009 Electrochemical behaviour of $(La_{1-x}Sr_x)_sCo_{1-y}Ni_yO_{3-\delta}$ as porous SOFC cathodes *Solid State Ion.* **180** 1395–405

[57] Ascolani-Yael J, Montenegro-Hernández A, Liu Q, Barnett S A and Mogni L 2019 Study of $La_{0.6}Sr_{0.4}Co_{1-x}Fe_xO_{3-\delta}$ (x = 0.2 & 0.8) electrochemical response as SOFC cathodes and its relation with microstructure *J. Electrochem. Soc.* **166** F1301–7

[58] Yakal-Kremski K, Mogni L V, Montenegro-Hernández A, Caneiro A and Barnett S A 2014 Determination of electrode oxygen transport kinetics using electrochemical impedance spectroscopy combined with three-dimensional microstructure measurement: application to $Nd_2NiO_{4+\delta}$ *J. Electrochem. Soc.* **161** F1366–74

[59] Baqué L, Caneiro A, Moreno M S and Serquis A 2008 High performance nanostructured IT-SOFC cathodes prepared by novel chemical method *Electrochem. Commun.* **10** 1905–8

[60] Garcés D, Wang H, Barnett S A, Leyva A G, Napolitano F R, Fuentes R O, Troiani H E and Mogni L V 2018 An insight into the electrochemical performance of $La_{0.5-x}Pr_xBa_{0.5}CoO_{3-\delta}$ as cathodes for solid oxide fuel cells: study of the O_2-reduction reaction *J. Mater. Chem.* A **6** 16699–709

[61] Montenegro-Hernández A, Mogni L and Caneiro A 2012 Microstructure and reactivity effects on the performance of $Nd_2NiO_{4+\delta}$ oxygen electrode on $Ce_{0.9}Gd_{0.1}O_{1.95}$ electrolyte *Int. J. Hydrog. Energy* **37** 18290–301

[62] Kremer J R, Mastronarde D N and McIntosh J R 1996 Computer visualization of three-dimensional image data using IMOD *J. Struct. Biol.* **116** 71–76

[63] Cronin J S, Wilson J R and Barnett S A 2011 Impact of pore microstructure evolution on polarization resistance of Ni-Yttria-stabilized zirconia fuel cell anodes *J. Power Sources* **196** 2640–3

[64] Chen-Wiegart Y C K, Demike R, Erdonmez C, Thornton K, Barnett S A and Wang J 2014 Tortuosity characterization of 3D microstructure at nano-scale for energy storage and conversion materials *J. Power Sources* **249** 349–56

[65] Caneiro A, Bavdaz P, Fouletier J and Abriata J P 1982 Adaptation of an electrochemical system for measurement and regulation of oxygen partial pressure to a symmetrical thermogravimetric analysis system developed using a Cahn 1000 electrobalance *Rev. Sci. Instrum.* **53** 1072–5

[66] Dellis J-L 2020 Zfit MATLAB Central File Exchange (available at: www.mathworks.com/matlabcentral/fileexchange/19460-zfit Accessed 8 June 2020)

[67] Hashimoto S I, Fukuda Y, Kuhn M, Sato K, Yashiro K and Mizusaki J 2011 Thermal and chemical lattice expansibility of $La_{0.6}Sr_{0.4}Co_{1-y}Fe_yO_{3-\delta}$ (y = 0.2, 0.4, 0.6 and 0.8) *Solid State Ion.* **186** 37–43

[68] Bouwmeester H J M M, Den Otter M W and Boukamp B A 2004 Oxygen transport in $La_{0.6}Sr_{0.4}Co_{1-y}Fe_yO_{3-\delta}$ *J. Solid State Electrochem.* **8** 599–605

[69] Garcés D, Leyva A G and Mogni L V 2020 High temperature transport properties of $La_{0.5-x}Pr_xBa_{0.5}CoO_{3-\delta}$ perovskite (x = 0, 0.2, 0.5) *Solid State Ion.* **347** 115239

[70] Nakamura T, Yashiro K, Sato K and Mizusaki J 2009 Oxygen nonstoichiometry and chemical stability of $Nd_{2-x}Sr_xNiO_{4+\delta}$ *J. Solid State Chem.* **182** 1533–7

[71] Montenegro-Hernández A, Vega-Castillo J, Caneiro A and Mogni L 2019 High temperature orthorhombic/tetragonal transition and oxygen content of $Pr_{2-x}Nd_xNiO_{4+\delta}$ (x= 0, 0.3, 1, 1.7 and 2) solid solutions *J. Solid State Chem.* **276** 210–6

[72] Montenegro-Hernandez A, Mogni L V and Caneiro A 2013 Validation of $Nd_2NiO_{4+\delta}$ as oxygen electrode material for intermediate temperature solid oxide cells with LSGM electrolyte *ECS Trans.* **58** 183–90

[73] Wilson J R, Sase M, Kawada T and Adler S B 2007 Measurement of oxygen exchange kinetics on thin-film $La_{0.6}Sr_{0.4}CoO_{3-\delta}$ using nonlinear electrochemical impedance spectroscopy *Electrochem. Solid-State Lett.* **10** 81–86

[74] Ding D, Li X, Lai S Y, Gerdes K and Liu M 2014 Enhancing SOFC cathode performance by surface modification through infiltration *Energy Environ. Sci.* **7** 552

[75] Jiang S P 2012 Nanoscale and nano-structured electrodes of solid oxide fuel cells by infiltration: advances and challenges *Int. J. Hydrog. Energy* **37** 449–70

[76] Lou X, Wang S, Liu Z, Yang L and Liu M 2009 Improving $La_{0.6}Sr_{0.4}Co_{0.2}Fe_{0.8}O_{3-\delta}$ cathode performance by infiltration of a $Sm_{0.5}Sr_{0.5}CoO_{3-\delta}$ coating *Solid State Ion.* **180** 1285–9

[77] Railsback J, Hughes G, Mogni L, Montenegro-Hernández A and Barnett S 2016 High-pressure performance of mixed-conducting oxygen electrodes: effect of interstitial versus vacancy conductivity *J. Electrochem. Soc.* **163** F1433–9

[78] Ullmann H, Trofimenko N, Tietz F, Stöver D and Ahmad-Khanlou A 2000 Correlation between thermal expansion and oxide ion transport in mixed conducting perovskite-type oxides for SOFC cathodes *Solid State Ion.* **138** 79–90

[79] Garcés D, Setevich C F, Caneiro A, Cuello G J and Mogni L 2014 Effect of cationic order-disorder on the transport properties of $LaBaCo_2O_{6-\delta}$ and $La_{0.5}Ba_{0.5}CoO_{3-\delta}$ perovskites *J. Appl. Crystallogr.* **47** 325–34

[80] Lu M Y, Scipioni R, Park B-K, Yang T, Chart Y A and Barnett S A 2019 Mechanisms of PrO_x performance enhancement of oxygen electrodes for low and intermediate temperature solid oxide fuel cells *Mater. Today Energy* **14** 100362

[81] Wang H, Zhang W, Guan K, Wei Z, Meng J, Meng J and Liu X 2020 Enhancing activity and durability of a-site-deficient $(La_{0.6}Sr_{0.4})_{0.95}Co_{0.2}Fe_{0.8}O_{3-\delta}$ cathode by surface modification with $PrO_{2-\delta}$ nanoparticles *ACS Sustain. Chem. Eng.* **8** 3367–80

[82] Zhu X, Ding D, Li Y, Lü Z, Su W and Zhen L 2013 Development of $La_{0.6}Sr_{0.4}Co_{0.2}Fe_{0.8}O_{3-\delta}$ cathode with an improved stability via $La_{0.8}Sr_{0.2}MnO_{3-\delta}$ film impregnation *Int. J. Hydrog. Energy* **38** 5375–82

[83] Sakito Y, Hirano A, Imanishi N, Takeda Y, Yamamoto O and Liu Y 2008 Silver infiltrated $La_{0.6}Sr_{0.4}Co_{0.2}Fe_{0.8}O_3$ cathodes for intermediate temperature solid oxide fuel cells *J. Power Sources* **182** 476–81

[84] Sažinas R, Andersen K B and Hansen K K 2020 Facilitating oxygen reduction by silver nanoparticles on lanthanum strontium ferrite cathode *J. Solid State Electrochem.* **24** 609–21

[85] Li M, Zheng M, Hu B, Zhang Y and Xia C 2017 Improving electrochemical performance of lanthanum strontium ferrite by decorating instead of doping cobaltite *Electrochim. Acta* **230** 196–203
[86] Zhou W, Ge L, Chen Z G, Liang F, Xu H Y, Motuzas J, Julbe A and Zhu Z 2011 Amorphous iron oxide decorated 3D heterostructured electrode for highly efficient oxygen reduction *Chem. Mater.* **23** 4193–8
[87] Dos Santos-Gómez L, Porras-Vázquez J M, Losilla E R, Martín F, Ramos-Barrado J R and Marrero-López D 2017 Stability and performance of $La_{0.6}Sr_{0.4}Co_{0.2}Fe_{0.8}O_{3-\delta}$ nanostructured cathodes with $Ce_{0.8}Gd_{0.2}O_{1.9}$ surface coating *J. Power Sources* **347** 178–85
[88] Ascolani-Yael J 2017 Study of the rate limitng steps and degradation of a $Ce_{0.8}Gd_{0.2}O_2$ impregnated $L_{0.6}Sr_{0.4}Co_{0.8}Fe_{0.2}O_{3-\delta}$ cathode *ECS Trans.* **78** 795–805
[89] Chen J, Liang F, Chi B, Pu J, Jiang S P and Jian L 2009 Palladium and ceria infiltrated $La_{0.8}Sr_{0.2}Co_{0.5}Fe_{0.5}O_{3-\delta}$ cathodes of solid oxide fuel cells *J. Power Sources* **194** 275–80
[90] Simner S P, Anderson M D, Engelhard M H and Stevenson J W 2006 Degradation mechanisms of La–Sr–Co–Fe–O_3 SOFC cathodes *Electrochem. Solid-State Lett.* **9** A478
[91] Koo B, Kim K, Kim J K, Kwon H, Han J W and Jung W C 2018 Sr segregation in perovskite oxides: why it happens and how it exists *Joule* **2** 1476–99
[92] Lee W, Han J W, Chen Y, Cai Z and Yildiz B 2013 Cation size mismatch and charge interactions drive dopant segregation at the surfaces of manganite perovskites *J. Am. Chem. Soc* **135** 7909–25
[93] Cai Z, Kubicek M, Fleig J and Yildiz B 2012 Chemical heterogeneities on $La_{0.6}Sr_{0.4}CoO_{3-\delta}$ thin films-correlations to cathode surface activity and stability *Chem. Mater.* **24** 1116–27
[94] Hong T, Lee S, Ohodnicki P and Brinkman K 2017 A highly scalable spray coating technique for electrode infiltration: barium carbonate infiltrated $La_{0.6}Sr_{0.4}Co_{0.2}Fe_{0.8}O_{3-\delta}$ perovskite structured electrocatalyst with demonstrated long term durability *Int. J. Hydrog. Energy* **42** 24978–88
[95] Hong T, Chen F and Xia C 2015 Barium carbonate nanoparticle to enhance oxygen reduction activity of strontium doped lanthanum ferrite for solid oxide fuel cell *J. Power Sources* **278** 741–50
[96] Cao X, Hong T, Yang R, Tian J, Xia C, Dong J and Li J 2016 Insights into the catalytic activity of barium carbonate for oxygen reduction reaction *J. Phys. Chem.* C **120** 22895–902
[97] Wang H and Barnett S A 2017 Sr surface segregation on $La_{0.6}Sr_{0.4}Co_{0.2}Fe_{0.8}O_{3-\delta}$ porous solid oxide fuel cell cathodes *ECS Trans.* **78** 905–13
[98] Tomov R I, Mitchell-Williams T, Gao C, Kumar R V and Glowacki B A 2017 Performance optimization of LSCF/$GdCeO_2$ composite cathodes via single-step inkjet printing infiltration *J. Appl. Electrochem.* **47** 641–51
[99] Tsvetkov N, Lu Q, Sun L, Crumlin E J and Yildiz B 2016 Improved chemical and electrochemical stability of perovskite oxides with less reducible cations at the surface *Nat. Mater.* **15** 1010–6
[100] Tealdi C, Ferrara C, Mustarelli P and Islam M S 2012 Vacancy and interstitial oxide ion migration in heavily doped $La_{2-x}Sr_xCoO_{4\pm\delta}$ *J. Mater. Chem.* **22** 8969–75
[101] Seymour I D, Tarancón A, Chroneos A, Parfitt D, Kilner J A and Grimes R W 2012 Anisotropic oxygen diffusion in $PrBaCo_2O_{5.5}$ double perovskites *Solid State Ion.* **216** 41–43
[102] Yashima M, Enoki M, Wakita T, Ali R, Matsushita Y, Izumi F and Ishihara T 2008 Structural disorder and diffusional pathway of oxide ions in a doped $Pr_2NiO_{4-\delta}$ based mixed conductor *J. Am. Chem. Soc.* **130** 2762–3
[103] Chem J M, Parfitt D, Chroneos A and Taranc A 2011 Oxygen ion diffusion in cation ordered/disordered $GdBaCo_2O_{5+\delta}$ *J. Mater. Chem* **21** 2183–6
[104] Kim I and Choi M 2019 First-principles study of anisotropic oxygen diffusion in $PrBaCo_2O_{5.5}$ *ACS Omega* **4** 10960–4
[105] Woolley R J and Skinner S J 2014 Functionally graded composite $La_2NiO_{4+\delta}$ and $La_4Ni_3O_{10-\delta}$ solid oxide fuel cell cathodes *Solid State Ion.* **255** 1–5
[106] Crumlin E J, Mutoro E, Ahn S J, La O G J, Leonard D N, Borisevich A, Biegalski M D, Christen H M and Shao-Horn Y 2010 Oxygen reduction kinetics enhancement on a heterostructured oxide surface for solid oxide fuel cells *J. Phys. Chem. Lett.* **1** 3149–55
[107] Sase M, Yashiro K, Sato K, Mizusaki J, Kawada T, Sakai N, Yamaji K, Horita T and Yokokawa H 2008 Enhancement of oxygen exchange at the hetero interface of $(La,Sr)CoO_3/(La,Sr)_2CoO_4$ in composite ceramics *Solid State Ion.* **178** 1843–52
[108] Sase M, Hermes F, Yashiro K, Sato K, Mizusaki J, Kawada T, Sakai N and Yokokawa H 2008 Enhancement of oxygen surface exchange at the hetero-interface of $(La,Sr)CoO_3/(La,Sr)_2CoO_4$ with PLD-layered films *J. Electrochem. Soc.* **155** B793
[109] Yashiro K, Nakamura T, Sase M, Hermes F, Sato K, Kawada T and Mizusaki J 2009 Composite cathode of perovskite-related oxides, $(La,Sr)CoO_{3-\delta}/(La,Sr)_2CoO_{4-\delta}$, for solid oxide fuel cells *Electrochem. Solid-State Lett.* **12** 135–8
[110] Gadre M J, Lee Y and Morgan D 2012 Cation interdiffusion model for enhanced oxygen kinetics at oxide heterostructure interfaces *Phys. Chem. Chem. Phys* **14** 2606–16